Review Vol. 8, No. 2 / February 2021 / Optica 161

Freeform optics for imaging

JANNICK P. ROLLAND,[1,*] MATTHEW A. DAVIES,[2] THOMAS J. SULESKI,[3] CHRIS EVANS,[2] AARON BAUER,[1] JOHN C. LAMBROPOULOS,[4] AND KONSTANTINOS FALAGGIS[2]

[1]The Institute of Optics, University of Rochester, 275 Hutchison Rd., Rochester, New York 14627, USA
[2]Dept. of Mechanical Eng. & Eng. Science, University of North Carolina at Charlotte, 9201 University City Blvd., Charlotte, North Carolina 28223, USA
[3]Dept. of Physics & Optical Science, University of North Carolina at Charlotte, 9201 University City Blvd., Charlotte, North Carolina 28223, USA
[4]Dept. of Mechanical Eng., University of Rochester, 275 Hutchison Rd., Rochester, New York 14627, USA
*Corresponding author: rolland@optics.rochester.edu

Received 29 October 2020; revised 15 December 2020; accepted 26 December 2020 (Doc. ID 413762); published 29 January 2021

In the last 10 years, freeform optics has enabled compact and high-performance imaging systems. This article begins with a brief history of freeform optics, focusing on imaging systems, including marketplace emergence. The development of this technology is motivated by the clear opportunity to enable science across a wide range of applications, spanning from extreme ultraviolet lithography to space optics. Next, we define freeform optics and discuss concurrent engineering that brings together design, fabrication, testing, and assembly into one process. We then lay out the foundations of the aberration theory for freeform optics and emerging design methodologies. We describe fabrication methods, emphasizing deterministic computer numerical control grinding, polishing, and diamond machining. Next, we consider mid-spatial frequency errors that inherently result from freeform fabrication techniques. We realize that metrologies of freeform optics are simultaneously sparse in their existence but diverse in their potential. Thus, we focus on metrology techniques demonstrated for the measurement of freeform optics. We conclude this review with an outlook on the future of freeform optics. © 2021 Optical Society of America under the terms of the OSA Open Access Publishing Agreement

https://doi.org/10.1364/OPTICA.413762

1. HISTORICAL HIGHLIGHTS

The earliest optical surface shape without rotational symmetry is the anamorphic lens, which uses toroidal surfaces with circular profiles but two radii along two orthogonal axes. This lens type was first used in periscopes during World War I to get a wider look outside of tanks. The Hypergonar lens, designed by Henri Chrètien in 1927 for photography and motion capture, revolutionized cinema in the 1950s [1]. In imaging applications, anamorphic surfaces defined as toroidal aspheres first took on the freeform denomination in a 2004 publication on all-reflective optical systems [2], heralding the emergence of more complex surface shapes than the conventional rotationally symmetric aspheres.

Progressive ophthalmic lenses pioneered the emergence of freeform optics in the marketplace and mass production [3]. Another early invention in ophthalmics is the Alvarez lens, which creates a variable focus using two cubic-shaped lenses displaced laterally relative to each other [4]. The Alvarez is still commonly used today to enable variable focus in visual instruments [5,6].

Another astonishing early entry of freeform optics in the consumer market came in 1972, in the viewfinder of the SX-70 Polaroid camera by James Baker and William Plummer and their collaborators [7]. Sales reached millions until 2005 when it was taken out of production. This team followed up with the Spectra camera also using "nonrotational aspheres" [8].

One type of emerging high-end imaging optics is a freeform three-mirror unobscured imager that leverages prior essential technology developments dating back to the late 1950s. In large part classified, this early work was driven by remote sensing by the government and scientific use. By the 1970s, designs began to become public in patents and peer-reviewed literature. Offner used off-axis conics sections to create afocal three-mirror anastigmats (TMA) for beam reduction [9]. Cook expanded that concept to a focal version of the TMA in 1979 [10]. In parallel, Wetherell and Womble developed a TMA without reimaging, now known as the reflective triplet [11]. Tatian and, independently, Shafer published some of the earliest designs with freeform surfaces in an unobscured three-mirror imager. Leonard conceived the Yolo telescope, where a toroidal secondary mirror was used for astigmatism correction in an unobscured three-mirror form [12]. Tatian used plane-symmetric $X-Y$ polynomials up to the 10th order, constructed upon a quadric surface [13]. Shafer used two-axis plate aspheres, also up to 10th order, with one decentered [14]. Optimization of three-mirror freeform solutions in the 1970s and 1980s was limited by available computational speeds and the lack of supporting aberration theory for design with freeform surfaces.

In imaging applications, Nakano and Tamagawa [15] and Fuerschbach *et al.* [16,17] sparked the next generation of freeform systems. While the development of TMAs has been a significant application driver of their work, the rise in freeform surfaces emerged first out of the need to create compact digital viewfinders for head-worn displays for augmented and virtual reality [18–22]. Bauer *et al.* demonstrated a high-end digital viewfinder for motion capture cameras with an all-reflective five-mirror geometry [23].

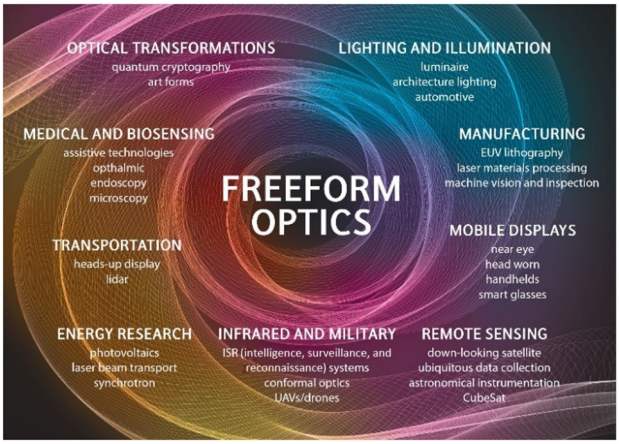

Fig. 1. Technology focus and market needs for freeform optics.

Figure 1 illustrates the opportunity for a wide range of applications associated with imaging and nonimaging optics alike. In lighting and illumination, freeform surfaces tailor the light from a specified light source to a prescribed illumination pattern at high efficiency [24–27]. Similarly, optical transformations leverage freeform surfaces for high-efficiency quantum cryptography [28]. In both applications with a common theme of illumination or sorting, the optics' precise shape is not as strictly defined as in imaging, where nanometer-scale precision is most often needed for aberration correction.

Today, the emergence of freeform optics has permeated remote sensing and military instruments [29–32], energy research [33], transportation [34], manufacturing [35], and medical and biosensing technologies [36]. Freeform optics have promise in both refractive and all-reflective unobscured systems. They both benefit from high performance and compactness, while all-reflective approaches provide the advantage of lightweight and achromatic solutions.

2. DEFINITION OF A FREEFORM SURFACE

Freeform surfaces can be defined as surfaces with no axis of rotational invariance (within or beyond the optical part) [37]. A freeform surface is illustrated in Fig. 2. This surface type requires and leverages three or more independent axes (e.g., the C-axis in diamond machining) to create an optical surface with as-designed asymmetrical features. In practical terms, in the context of design, a freeform surface may be identified by a comatic-shape component or higher-order rotationally variant terms of the orthogonal polynomial pyramids, themselves independent so they can be "dialed-in" at will. These components often come together with an astigmatic surface component. In simple terms, in design, freeform surfaces go beyond spheres, rotationally symmetric aspheres, off-axis conics, and toroids. Let us note that an off-axis conic is not a freeform surface because two axes are sufficient to fabricate and measure it. However, in some cases, making the conic with three axes is more practical. A toroid is a freeform in fabrication and metrology and may serve as a freeform base surface in design.

Mathematical descriptions of freeform surfaces may be local or global. Radial basis functions [38], basis splines [39], wavelets [40], non-uniform rational basis splines [41], and hybrid stitched representations are local descriptions investigated in optical system design [42]. Orthogonal polynomials, specifically Zernike and $2D-Q$ polynomials, are commonly chosen global descriptions

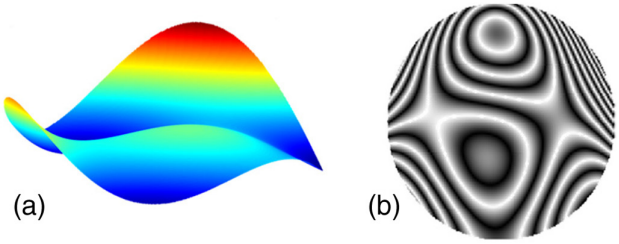

Fig. 2. Freeform surface: (a) 3D plot and (b) simulated interferogram.

[43–45], while non-orthogonal bases such as $X-Y$ polynomials are also common practice [46]. Ye *et al.* provided a recent review of the mathematical descriptions for freeform surfaces [47]. Regardless of the specific definition, freeform surfaces, including those consistent with Eq. (A.1) in ISO 10110 Part 19, typically have a sag equation separable into a base surface and a sag departure [48]. It is worth noting that the base surfaces' sag's magnitude often significantly exceeds the freeform sag departures. Minimizing the freeform sag departures while meeting the design specifications is highly desirable as it has key implications in both fabrication and metrology [49]. Toward this goal, it has been shown that the advantages of orthogonal polynomials are best leveraged by understanding the interactions between variables that cause degeneracy [50]. Optimization constraints may then be used in design to break these degeneracies and yield more optimal designs from a manufacturing viewpoint [45]. The choice of a base surface has been shown to play a critical role in outcome metrics for testability [51]. Specifically, the authors show that choosing an off-axis conic as the base surface in place of a base sphere, upon which orthogonal polynomials in both cases define the freeform departure, yield an order of magnitude improvement in testability estimates.

3. CONCURRENT ENGINEERING

The community has long recognized the disadvantages of a serial design process in optical system development. Yoder (1986) quotes Johnson's conviction (in 1943) that "in the design of any optical instrument, optical and mechanical considerations are not separate entities, to be dealt with by different individuals" [52]. Kasunic (2015) documents that there can still be a chasm between optical and mechanical design tasks [53]. He states that "the lens designer's deliverable to the optomechanical engineer is a toleranced prescription with alignment and fabrication analyses developed in coordination with the optomechanical engineer; in practice, this is not always done." Johnson's and Kasunic's comments reflect a potential problem area and, indeed, a common challenge in developing state of the art on-axis systems. Experience with off-axis, freeform techniques demonstrates that more than "coordination" between optical and optomechanical design is needed. The entire engineering process must be concurrent.

The concurrent engineering concept is taught to undergraduate engineering students in mechanical engineering and manufacturing engineering programs [54]. Simply, that approach espouses all parts of the product development enterprise's simultaneous involvement in a parallel effort. We should consider optical design for manufacture and assembly [17,55], metrology [51,56], and cost throughout the development process.

In 2017 in a snap-together freeform TMA, Horvath *et al.* demonstrated that concurrent engineering of a freeform optical system requires complex interactions between disciplines [57]. A

freeform optical design can be remarkably compact, as previously described. However, space must be included for opto-mechanics, position adjustment mechanisms for tuning and, for imaging, to incorporate a detector and its housing. Tradeoffs between form tolerances on the optics and positioning tolerances should also be thoroughly considered as the cost differential between an ultra-precision machine, described here, and a more conventional precision machine can be substantial (i.e., hundreds of dollars per hour or more). Thus, what appears to be a simple decision in an optical design can have ramifications for all aspects of the system development and can significantly affect the overall system cost.

A universal example of design for manufacture with freeform components, linking design to fabrication and test, establishes the best way to tolerance surface shapes using either individual surface polynomial terms or standard or new methods. Traditional tolerancing concepts embodied in optical design software and ISO standards of "irregularity" seem questionable for freeform optics. Designers can specify surface form tolerances based on contributions of some bandwidth-limited combination of Zernike or other polynomials [48]. But is this generally useful? For adaptive optics systems with active "mirror benders," it makes sense to tolerance low-order figure error based on the uncertainties associated with the correction's spatial bandwidth. From the perspective of optical system performance, it is not clear that tolerances based on a root sum squared (RSS) combination of a bandwidth-limited set of polynomials makes sense. The RSS implies uncorrelated error sources. But are the error contributions from the manufacturing process uncorrelated? They are not. For example, diamond turning tool errors (i.e., waviness) that generate symmetric error patterns mapping to the rotationally invariant polynomial terms (spherical Zernike terms) are correlated. Similarly, in coordinated axis turning of freeform optics, the controller's dynamic response leads to non-axisymmetric errors that map to the asymmetric Zernike terms, again correlated. For these examples, an RSS combination of a bandwidth-limited set of polynomials is not sensible.

In a similar direction, the optomechanical design of thin, curved freeform or conformal optical components needs to account for bending deformations. Specifically, following the manufacturing of one surface, highly localized, non-uniform bending deformations are expected to occur near free or supported edges in a boundary layer, affecting the component aperture and tolerances. The boundary layer's extent depends on the component curvature and thickness [58]. Methods to estimate the tolerances associated with optomechanical components whose thicknesses or curvatures are highly position dependent are still needed.

Designers must consider the sensor package size and position early in the process; adapting spacing to adjust the detector position in the optical system may minimize total volume. Similarly, a minimum volume can be reached without ray obscuration by considering the aperture sizes and mechanical mounting features.

Monolithic systems or systems with multiple surfaces on a single substrate (including freeform prisms) require early discussion of optical design, manufacturing, and metrology. The advantage stems from the fabrication machine's accuracy, setting the optical elements' positioning, and reducing assembly. The disadvantages include the need for reach and access yielding increased component sizes, translating to the increased effect of machine-induced geometric errors, and longer manufacturing times prone to associated thermal drift. The advantages and disadvantages should be weighed against component performance and cost, further emphasizing the need for concurrent engineering.

Design for assembly focuses on using kinematic locations in *snap-together* components that mitigate the added complexity of multiple adjustments [17,57]. Tolerances on the fabrication of reference, datum, fiducial, or kinematic locating surfaces can translate into reduced surface tolerances. Multiple platforms from manufacturing to metrology to final assembly may adapt kinematic alignment systems so that manufacturability can be repeatable, measured, tested, and corrected in a closed-loop methodology [55]. Adjustments, while still often needed, are then minimized. The ideal optic for adjustment is the one that provides sufficient optical performance recovery with the most straightforward mechanical interface.

These examples point to a system production process that may differ from most current practices. Currently, optical designers specify the form and locations of the individual optics. Simultaneously, the degrees of freedom for adjustment are maximized to compensate for all possible manufacturing and assembly errors. This approach is a proven process for traditional on-axis designs. However, the challenges and the advantages of freeform optics and systems make the concurrent engineering approach much more advantageous and, in most cases, essential. Bauer *et al.* described that an optical designer's best practice might begin with a suitable set of starting geometries [59]. The design form is then overlaid on fabrication and metrology platforms' capabilities while considering optomechanical assembly. Because freeform optics exercise all error sources in the manufacturing platform, the designer can model these errors. Specifically, working with the manufacturer, the optical designer then tailors the optical design to minimize, a priori, the effects of these error sources on optical performance. In essence, the optical design is made less sensitive to these errors. The same analysis is repeated for assembly errors. Here, we consider component metrology and system performance testing simultaneously. Metrology fiducials and mechanical locating features are designed accounting for the dominant sources of manufacturing and assembly errors, and the effects of these errors on system performance. Finally, we consider the essential adjustment degrees of freedom needed to recover system performance in final testing. The design is then again optimized, before production, based on all available information. Note that a concurrent-design approach results in a deterministic and repeatable fabrication process. A monolithic system is an extreme case where compensation is a part of the design, prototyping, and initial metrology and testing. In production, process repeatability ensures final quality.

4. REVIEW OF DESIGN METHODS

The wave aberration theory of H. H. Hopkins is the foundation of optical design for rotationally symmetric systems [60]. In the mid-1970s, Shack and Thompson expanded this theory into Nodal Aberration Theory (NAT) to account for misaligned systems [61], leveraging the *sigma vector* insight from Buchroeder [62]. Specifically, NAT uses decenter and tilt values to calculate the displacement of the aberration fields produced by each optical surface characterized by a sigma vector [63,64]. The sum of the displaced aberration fields results in cancellations within the field of view, referred to as nodes, hence NAT's name. Thompson then fully developed NAT to fifth order [65–68], laying a foundation for the aberration theory of freeform surfaces. The essence of how aberrations evolve with asymmetry, regardless of their types, are

summarized perhaps surprisingly: the aberration types remain the same; the novelty is in their field dependence.

Building on NAT, Fuerschbach *et al.* developed the aberrations theory for freeform surfaces [69]. Specifically, a freeform surface placed at the optical system's aperture stop creates field-constant aberration of that freeform type. For example, a surface shape with Zernike coma located at the aperture stop will induce field-constant coma. Away from the aperture stop, the aberrations' field-dependencies created are multiple and unique to each surface shape. A Zernike coma shape placed away from the aperture stop will generate field-asymmetric field-linear astigmatism, field-asymmetric defocus equivalent to image tilt, and field-constant coma. Considering the first 17 FRINGE Zernike terms revealed six different field dependencies of astigmatism, one example of the increased complexity from utilizing freeform surfaces away from the aperture stop.

Building on the theory of aberrations for freeform surfaces, Bauer *et al.* developed a method for designing with freeform optical surfaces [59]. As in every optical design, the first challenge is creating a viable starting point. Bauer's approach includes a taxonomy of starting-point geometries that accounts for manufacturability. Their hierarchy reflects their potential to be corrected from optical aberrations after using freeform surfaces. Contrary to methods adopted prior to this work, where a best practice was to create a rotationally symmetric starting point corrected to third order, Bauer instead only ensures first-order properties, then unfolds the system, and finally focuses on analyzing the optical aberrations to classify the starting unfolded geometry in the taxonomy. Bauer demonstrates the method's effectiveness in designing a multiple mirror imager. Given the constraints of design problems, the optimal geometry is at least 16 times better than the worst geometry, which underscores the geometry's importance. Building on that method, a weighted square-sum of the polynomial coefficients used to describe the freeform surface defines a "spheroid" of manufacturability, in the case where the base surface is a sphere. This square sum can be added as a soft constraint to the optimization error function to minimize manufacturability metrics [45]. Similarly, an "ellipsoid" of manufacturability targeted at subaperture stitching metrology was described in [70]. Here, the local surface is typically dominated by astigmatism that is nulled out, which is also suitable for on-the-fly constraints in optimization.

Sasian also undertook another expansion to the H. H. Hopkins theory in the context of off-axis plane-symmetric systems [71]. The approach enables investigating unobscured off-axis systems such as TMAs with off-axis conics. Sasian's formulation requires careful handling of coordinate systems. In his process, one follows the Optical Axis Ray (OAR) and breaks symmetry only with tilts and no decenters, which is similar to the perspective taken in Hamiltonian optics that follows the basal ray and defines optical surfaces about the intersection of the basal ray with the surface [72,73]. Reshidko and Sasian extended the approach to include freeform surfaces [74], and a method for confocal mirror designs also emerged [75]. Papa *et al.* combined aberration theory insights from designing with off-axis confocal-conic mirrors and conventional third-order aberration correction to yield starting points analytically corrected through the third-order aberrations [76]. This work has enabled automated surveys of the freeform reflective imager solution space [77].

Taking a radically different approach, the *Simultaneous Multiple Surface* (SMS) method, developed initially as a nonimaging optics tool [78], forgoes using a conventional ray trace optimizer. Instead, SMS solves for N surface shapes that transform N input wavefronts into spherical wavefronts in image space. This method essentially creates N perfectly corrected field points and makes systems aplanatic [79]. Yet, in another radically different approach to design, driven by the pursuit of minimizing human interaction, Yang *et al.* used a point-by-point method wherein a point-cloud determines the surface shapes and best satisfies Fermat's principle for featured rays traced through the system. The surfaces are then fit using a polynomial set, and the process is repeated [80].

5. FABRICATION METHODS

Since freeform surfaces lack an axis of rotational invariance, their fabrication requires more than two degrees of freedom typical for conventional methods, with material removal via a sub-aperture mechanism [37]. These two common characteristics of freeform fabrication introduce challenges. Each additional degree of freedom adds error sources and increases the complexity of motion control [81]. Sub-aperture removal increases the fabrication time and introduces mid-spatial frequency (MSF) errors. Thus, error sources occur across a wide range of spatial wavelengths from figure to surface roughness, with processes applied to a wide range of materials, ductile and brittle, reflective and transmissive. The sub-aperture interaction zone affects the mechanisms of material removal. The main freeform fabrication processes are ultra-precision machining, loose abrasive or bound abrasive finishing, molding/replication, and novel processes.

Ultra-precision Machining. Ultraprecision machining is an enabling technology for freeform optics. The root technology was single-point diamond turning, the manufacture of a component on a precision lathe (turning) with one crystal diamond tool developed over the past 125 years. In the first half of the 20th century, metal cutting tools included diamond tools for non-optical components [82] and scientific instrument manufacturers [83].

The first single-point diamond turning of optical-level components was driven by military applications in World War II [84]. In the 1950s, Bell and Howell with Moore Special Tool Company developed a high-precision three-axis aspheric generator with computer numerical control (CNC) and error compensation. Turned components included a germanium aspheric lens for a forward looking infrared (FLIR) imaging system and aspheric aluminum mirrors for an infrared Cassegrain telescope [85].

The U.S. weapons laboratories made significant developments in diamond turning. Oak Ridge used polished single-crystal diamond microtome knives [83,84,86]. Other labs customized turning platforms, with the first commercial machines emerging in the late 1970s for axisymmetric components [87,88]. Fast-tool-servo (FTS) introduced the third degree of freedom, coordinating linear motion (e.g., X, Z) with rotation (C), as shown in Fig. 3(a) [89].

Modern ultra-precision freeform machining can use multiple geometric configurations to move the diamond tool relative to the surface. While Fig. 3(a) shows an FTS system explicitly, this configuration is generally referred to as coordinated axis turning. In modern systems with linear motor drives, an FTS is not required to coordinate the motion of X and Z with C. Other configurations allow more versatility in cutting freeform surfaces. In three-axis milling or grinding, as shown in Fig. 3(b) and Fig. 3(c), a rotating tool moves relative to the optical substrate with three degrees of freedom (X-Y-Z). More complex surfaces may require additional

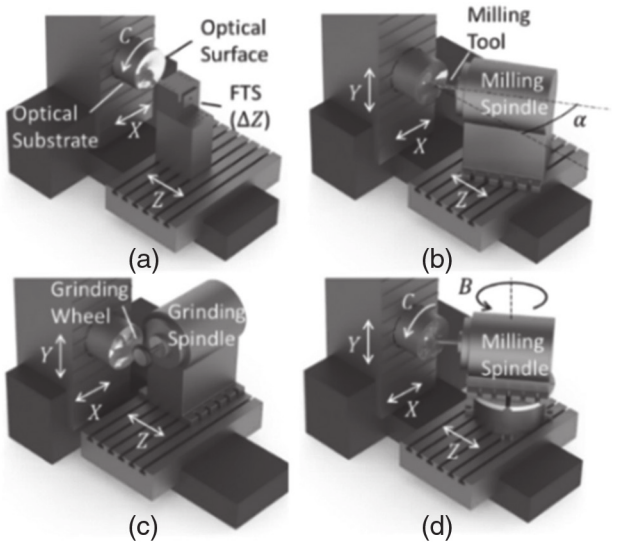

Fig. 3. Geometric characteristics of ultra-precision machining processes: (a) coordinated-axis diamond turning ($X-Z-C$), (b) three-axis milling ($X-Y-Z$), (c) three-axis grinding ($X-Y-Z$), and (d) five-axis milling ($X-Y-Z-B-C$).

degrees of freedom: Fig. 3(d) shows five degrees of freedom (X-Y-Z-B-C), three rectilinear motions, and two rotations in a five-axis milling configuration.

The choice of the machining configuration goes beyond geometric design. In coordinated-axis diamond turning without an FTS, typical workpiece rotation rates are low because of the machine axis motions' bandwidth. When using only the machine axes for moving linearly, the rotation of C is typically below 300 revolutions per minute (rpm). The X and Z motion speeds are on the order of tens of mm per minute, so the fabrication time is high (i.e., many hours for a ∼100 mm clear aperture optic). An FTS produces small but high bandwidth modifications to the Z position (ΔZ), typically at frequencies up to 1 kHz but with limited magnitude (∼ 1 mm)). If these smaller amplitude motions are suitable for a given component, the rotation rates can be increased by more than an order of magnitude. There are commensurate reductions in manufacturing time [90].

A limitation of coordinated axis machining is the tool's tip's ability to reach all features of a surface without collisions, known as *reach and access*. When reach and access are an issue, milling can be more versatile: a small diameter tool (i.e., generally <3 mm), rotating at high speed (i.e., >10,000 rpm), is moved with three to five degrees of freedom, and it removes the material. The tool rotation is stand alone, with other axes or rotational motions moving independently. The rotating tool edge generates a volume of revolution (i.e., typically spherical or toroidal), thus removing material. Linear (e.g., X, Y, and Z) or rotational (e.g., B and C) movements can produce the required motion of the tool relative to the material. Using more than three degrees of freedom provides for more complex cutting paths (e.g., undercuts). The tradeoffs are additional sources of error.

Modern machines are designed to have precise motions to reduce errors. Rotational spindle error motions (i.e., radial and axial) are <10 nm peak-to-valley (PV), with an angular resolution of 1.75 nrad. In turning, spindle error motions induce MSF-surface structures. Linear motors pilot linear axes, supported by hydrostatic ways, with better than 1 nm resolution with position measurements. The instrument's resolution contributes to the overall error that includes other effects. Specifically, the geometric accuracy in linear axes is about a fraction of a micron, while thermal effects may be more significant. Uncorrelated errors combine in quadrature at each point, varying in the machine workspace. Current research concentrates on predictive error models for three- to five-axis machines [91].

Compared to a single crystal diamond cutter, a grinding tool allows more brittle materials to be cut and shaped. The tool-cutting edges are no longer precisely defined, and the wheel wears, naturally changing shape during grinding, leading to tool-shape-added errors.

Thermal, elastic-fixturing, and tooling error sources exemplify freeform optics machining errors [92]. Repeatable mechanical errors are compensable, as are steady-state thermal errors. Non-repeating errors such as transient thermal effects, tooling, and fixturing remain after compensation. Temperature control can mitigate thermal errors. At Lawrence Livermore National Laboratory, the large-optics diamond-turning machine (LODTM), arguably the most accurate machine tool ever made, could accommodate the manufacturing of optics up to 1.6 m in diameter with a 500 mm sag [88]. Figure error on highly aspheric optics is <10 nm root mean square (RMS) over its full swing. This achievement required incorporating multi-path laser feedback, capacitance gauges, computer control of capstan drives actuating the two axes, vibration isolation, and strict temperature control, including that for water.

No current machine matches this capability, and few have the resources to recreate LODTM. With more affordable thermal environments (±0.1°C) and commercial equipment, figure errors on large freeform optics (i.e., >500 mm clear aperture) are on the order of 1 μm, and errors typically scale with the optics size and cutting time.

Early freeform optics applications have been in the infrared because surface finish and tolerance requirements are less demanding [16,17,93]. Applications have expanded to include shorter wavelengths. As shown in Fig. 4, Owen *et al.* developed compensation techniques for the dominant tool error sources on a small, extreme freeform optic with a clear aperture of 5 mm, a departure from the base sphere of 0.352 mm, and a maximum slope of 26.5° [92]. The procedure utilized test spheres to mitigate three dominant error sources in freeform milling: tool decenter, tool radius, and tool waviness. The errors were modeled and mapped by milling test spheres shown in Fig. 4(a). The mapping was verified by compensating the sphere cutting tool path, reducing the figure errors on the spheres from 839 nm to 269 nm PV. The remaining errors were from non-repeatable thermal cycling. The same tool model was then used to cut a 3 mm test freeform with a 132 nm PV error (see Fig. 4(a)) and 332 nm PV error on the final optic. Figures 4(b) and 4(c) show the model and the actual part. Figure 4(d) shows the freeform profile of the manufactured part. Figure 4(e) exemplifies dominant remaining errors, specifically MSF errors with a spatial wavelength of approximately 0.6 mm and an amplitude of about 200 nm from the cycling of the machine's spindle temperature thermal control systems. Current methods for compensating these errors combine on-machine monitoring (e.g., thermocouples) with predictive modeling for dynamic real-time compensation [94].

Sub-micrometer form errors in diamond machining were attainable in the previous example because of the optics' small

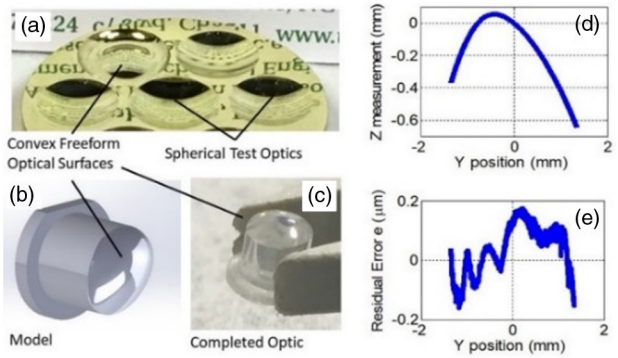

Fig. 4. (a) Diamond-milled test spheres and test freeform surface in C46400 naval brass, (b) computer model of the optic, (c) completed optic, (d) form Talysurf trace of the optical surface, and (e) residual error from the prescription.

clear aperture. Larger freeform optics for astronomical applications utilize more machine workspace and are more sensitive to geometric machine errors, temperature, and thermal gradients. In 2005, Saunders *et al*. reported freeform mirrors integrated into the James Clerk Maxwell Telescope [95]. They alluded to needing concurrent engineering. They used an on-machine linear variable differential transformer system, precise in linear displacement down to 25 nm, to perform on-machine metrology during the coordinated-axis diamond turning of freeform aluminum optics. They reported a figure error of 5.7 μm PV and surface roughness of 15 nm RMS on a 650 mm optic, suitable for applications across the range of longer wavelengths (i.e., 200 μm–1 mm). We will further discuss on-machine metrology in Section 7.

Beier *et al.* designed a compact four-mirror freeform telescope, where the mirrors M1/M3 and M2/M4 pairs were flycut with an FTS coordinated-axis system [96]. Given apertures ranging in size from 20 mm to 160 mm, they report surface roughness <10 nm RMS and figure errors of 0.5–1.0 μm mainly caused by thermal variations. As in Owen *et al.* [97], the authors also use a milling spindle to machine kinematic alignment features on the optics in the same setup as the optical surface machining. Horvath *et al.* adapted the tool correction methods proposed by Owen *et al.* and the simultaneous milling of kinematic alignment features to manufacture the snap-together, 83 mm aperture, freeform TMA system shown in Fig. 5 [57,92]. The errors on these surfaces and the assembly combine to produce approximately 1.25 μm PV wavefront error. However, wavefront variations due to assembly/disassembly were much lower, around 25 nm PV, implying a further reduction of machine error sources would enable consistent system production. Li *et al.* extended this concept to a fully monolithic freeform system machined in a single setup. These results suggest that figure errors and RMS roughness on freeform optics across various length scales can be <1 μm PV and <5 nm RMS, respectively [98].

Diamond machining can produce optical-level surface roughness materials without prohibitive diamond wear. These include ductile metals such as copper, aluminum, brass, and electroless nickel, many plastics, and also brittle materials such as germanium, zinc selenide, and zinc sulfide. Smilie *et al.* first demonstrated the freeform milling of an infrared Alvarez lens in germanium [93]. Owen *et al.* and Troutman *et al.* showed that chalcogenide glass and germanium could be freeform milled at high speeds, fabricated, and tested, while also demonstrating the simultaneous milling of an optical surface and kinematic alignment features [97,99].

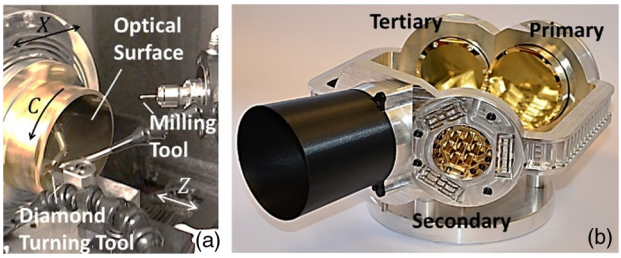

Fig. 5. (a) Diamond-turning of the primary mirror surface and simultaneous milling of kinematic mounting spheres to enable a (b) snap-together freeform TMA with 83 mm aperture and ±2° FOV. (Adapted from [57].)

The machining of brittle materials requires both surface and subsurface integrity [100]. Finally, diamond machined surfaces have a non-isotropic structure (i.e., a spiral pattern for turning and a linear grating pattern for milling). Consequences and mitigation strategies are discussed in more detail in Section 6.

Finishing. Beyond turning or milling, we also consider subaperture finishing processes, where two operations are needed to remove material. First, a material removal mechanism produces a deterministic footprint on the optical surface, depending on the material type and the processing variables [101]. The three-dimensional (3D) geometry of the footprint is measured. Second, the footprint removal rate is convoluted with a specified tool path and dwell time over the part surface to produce a desired overall removal [102]. Optimization of the tool path and dwell time is critical in software inverting the convolution [103], especially when additional constraints are imposed (e.g., edges [104], or low accelerations [105]).

Subaperture finishing must consider the extent of subsurface damage removal [106]; residual in-plane surface stresses [107]; microroughness [108,109]; material microstructure (grains vs. grain boundaries [110,111]; two-phase materials [112]); edge effects [58,104], and MSF errors [113]. A recent review of materials issues can be found in Suratwala [114].

Different material removal mechanisms reflect the optical surface's interaction with solids, liquids, smart fluids, energetic atomic species, or light. In all mechanisms, a generalized *Preston-like* equation describes how material removal rate (MRR) depends on a set of process variables, process time, and a material-and-process-dependent coefficient [115].

The most traditional approach involves solid contact of a compliant tool, with bound abrasives with abrasive belts [116,117] or bonnets [118] and the optical surface. The stiffness of the contact affects the MRR. Contact along the surface normal leads to material removal driven by surface tangential shear stresses. Due to the stiff tool Hertz-like contact with the surface, these approaches typically require more stringent positioning of the tool.

Another approach removes material via interaction with a fluid such as water jet polishing with a nozzle [119]. A similar method uses a magnetorheological (MR) fluid that rapidly converts from fluid to solid-like under a magnetic field [120,121]. The magnetorheological finishing (MRF) process produces a non-wearing material-removing lap. A further development uses an MR fluid jet delivered via a nozzle and under an applied magnetic field, leading to a highly stable and deterministic MR jet [122]. In all cases, surface shear stresses drive the material removal rate.

Yet another means of material removal is the interaction of the surface with energetic particles, as in ion beam figuring [123],

or reactive atom plasma processing [124], where non-thermal ablation drives material removal. The presence of a vacuum chamber and the slow removal rate must be offset by reduced microroughness.

A more recent approach is fs-laser polishing [125]. Optimizing processing variables is critical (laser repetition rate, energy per pulse, pulse overlap, and scan speed) to promote non-thermal annealing and avoid melting or oxidating the material. A two-temperature model for the electron and lattice temperatures may guide optimization. A key result is establishing the ablation threshold [126].

Mitigation or removal of MSFs is neither trivial nor universally demonstrated. Specification and metrology of MSFs are essential (see Sections 6 and 7).

Replication. In addition to the processes above, replication is a path to a low-cost proliferation process, now briefly outlined.

For nonimaging or imaging optics with loose tolerance requirements, plastic molding is achievable with proven low-cost technologies [127]. For imaging systems, precision glass molding (PGM) is the leading technology for volume production [128]. The molds are manufactured using technologies discussed earlier in this section. Mold life and performance depend on the properties of the mold material and its surface integrity. Requirements of mold materials are hardness, thermal stability, and chemical resistance. Examples are tungsten carbide and advanced ceramics, ground to shape on an ultraprecision machine, and then finished. Freeform optics molding brings up the same challenges as in direct-machining: more than three degrees of freedom fabrication technology, in-process metrology, verification metrology, surface roughness, and MSF errors. Departure from axial-symmetry makes error prediction and correction in the molding process more challenging. Gurganus *et al.* have recently reported on a large (>40 mm clear aperture) high-aspect-ratio freeform Alvarez lens produced by PGM with <3 nm RMS surface roughness and <8 μm form error [129]. Improvements are necessary for visible optics. Mold errors cause correctable form errors.

6. SPECIFYING MID-SPATIAL FREQUENCY ERRORS

As briefly discussed in the previous section, MSF surface errors are common byproducts of computer-controlled sub-aperture manufacturing techniques necessary to fabricate freeform optics. However, they can degrade optical performance [130,131]. Surfaces manufactured with sub-aperture turning, milling, grinding, and polishing leave residual surface textures with signatures characteristic of the fabrication processes [132,133]. Sources of these errors include tool shape, tool wear, tool path, vibrations, mechanical runout, thermal changes, and material properties [134–136]. Standards for optical surface textures [137] are "primarily intended for the specification of polished optics," and care must be taken if used with "materials having a crystal structure and production processes" (such as diamond machining) that "give rise to non-random surface texture."

The range of frequencies identified in the literature as MSF is somewhat fluid. The default range of spatial wavelength for "waviness" in specification standards ranges between 80 μm and 2.5 mm [137]. Aikens *et al.* have proposed the MSF range as being between "low" frequency errors specified by a 37 term Zernike polynomial expansion and "high" spatial frequencies where the Fresnel lengths ($L_f = a^2/\lambda$, where a is the spatial length scale of the surface error) of the patterns are "<1/10th of the optical path distance from a given surface to the image plane" [138]. MSF errors diffract light outside the central point spread function (PSF) peak, but at angles small enough to illuminate the image plane directly. In contrast, low-frequency form errors alter the height of the PSF, and high-frequency roughness errors scatter light at large angles [139]. Functionally, the spatial scales of roughness and MSF are wavelength dependent.

Understanding the impact of MSF errors on optical performance is of utter importance. MSF errors are equivalent to conformal diffraction gratings or phase screens superimposed on the base optical component. Point cloud representations or high-order surface fits using basis sets such as Forbes [140] or Zernike polynomials [141], or radial basis functions [142] may represent MSF surface data. Each approach can impact modeling and simulation. The dimensional scales and (quasi) periodic nature of MSF errors motivate the use of physical optics concepts for accurate simulation and modeling, which can be computationally challenging [143]. These challenges encourage approximations and simplifying assumptions such as ray-tracing enabled using lower-order surface fittings to the residual MSF surface errors. These approaches facilitate simulation of MSF errors' impacts on optical performance for multi-element optical systems but at the risk of information loss from higher-order fit terms [144]. Liang *et al.* recently explored the perturbation model's validity to facilitate modeling MSF errors' impacts on optical systems [145].

The magnitude of MSF errors can be reduced using extreme care during the original manufacturing process or mitigated using post-processing methods. These approaches can be costly and time-consuming. A leading question then becomes, "How much MSF surface error is acceptable?" The answer depends on the application, the MSF texture pattern, and the surface location relative to the exit pupil and image plane. Specification methods for MSF surface errors with clear connections to optical performance provide quantitative guidance to avoid over-specifications that increase cycle times and cost.

There are multiple common surface specifications: peak to valley (PV), bandlimited RMS departure, RMS gradient or normal gradient departure (i.e., "slope"), power spectral density (PSD) [146], and the structure function [147]. Common metrics for optical performance include the RMS wavefront error or closely related Strehl ratio, modulation transfer function (MTF), and encircled energy radius (EER) [148]. Early studies on the effects of sub-aperture fabrication tool errors are statistical. They date back to evaluating residual surface roughness of diamond machined optics by Church and Zavada [149] and Stover [150] as special cases of scattering theory. Impacts on image quality from random MSF surface errors and structured rotationally periodic waviness were considered by Noll [151] and Marioge and Slansky [152], respectively. Youngworth and Stone [153] developed simple estimates for MSF errors' effects on image quality based on RMS surface departure, assuming isotropic error distributions. Tamkin and Milster reported the impacts of structured MSF errors on image performance [154]. Tinker and Xin [155] demonstrated an empirical correlation between the RMS surface gradient and EER for fast aspheres. More recently, Alonso and Forbes [156] and Liang and Alonso [157] presented semi-analytical methods to estimate the effects of MSF errors with idealized geometries on Strehl ratio and MTF, respectively, and Aryan *et al.* revealed direct

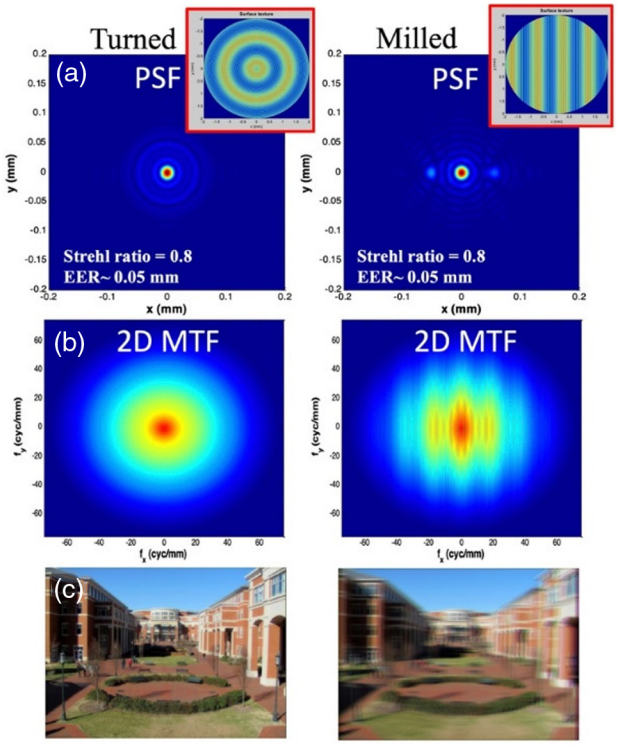

Fig. 6. Simulated outputs from a simple lens with (left) diamond-turned and (right) raster-milled surfaces that have the same nominal surface statistics but different optical performance: (a) Rayleigh–Sommerfeld PSF, Strehl ratio, and EER; (b) 2D MTF, (c) images [160].

connections between diamond-machining parameters and the Strehl ratio [158]. Until recently, optical surface textures' specification standards have primarily assumed isotropic error distributions and leveraged bandlimited RMS departure and one-dimensional PSD [159,160]. Recent updates to the standard provide additional flexibility [137].

A key observation is that MSF errors may not be isotropic over an aperture, resulting in significant optical performance differences from surfaces with similar conventional surface statistics. Figure 6 shows a simple lens with two different synthetic MSF signatures resulting from diamond tool shape, tool path, and thermal changes. These MSF signatures have the same nominal PV, RMS departure, RMS slope, and linear structure function. The Strehl ratio and EER do not clearly distinguish between the two surfaces, but the two-dimensional (2D) MTF and the imaging performance are visually different.

This example illustrates some challenges in specifying MSF surface errors. PV, RMS departure, and RMS slope are simple numbers that are easy to understand and determine "pass/fail" criteria. Still, they do not retain information about either the distribution or anisotropy of surface errors. The area structure function [161] and 2D PSD include anisotropy information. Yet, they are not easily connected to optical performance criteria, are more complex to interpret and set specifications, and are thus less likely to be used in practice. In particular, the 2D PSD contains extensive information about the surface. Still, when averaged over orientation to a 1D representation (e.g., horizontal, vertical, or azimuthal), it loses information about surface anisotropy. The 2D MTF quantifies anisotropic optical performance but is less common than simple 1D cross-sections [162].

Toward these challenges, Forbes has introduced an orthogonal basis set that provides promising options for specification and analysis of MSF structures [140]. Petermann *et al.* introduced a novel polar representation of the 2D PSD to characterize anisotropic MSF signatures [163]. Aryan *et al.* recently introduced a new metric that captures the minimum optical modulation from the 2D MTF and presents it in the more commonly used 1D format [164]. Aryan also demonstrated a method to estimate optical performance and set acceptance criteria for surfaces with anisotropic MSF errors [165]. There are opportunities for additional research to develop and refine appropriate specification methods and standards for generalized MSF surface errors.

Mitigation of MSF Errors. Mitigation of MSF surface errors has been achieved by several approaches. For example, pseudo-random tool paths can be used during fabrication to reduce the surface errors' structured nature, minimizing dominant amplitude peaks in the surface PSD [166]. Use of inverse corrector optics has been demonstrated for minimizing the impacts of MSF errors [167]. Surfaces fabricated with deterministic tool paths giving rise to dominant peaks in the PSD can be post-processed to reduce the amplitude of the MSF surface errors, which reduces the amplitudes of the PSD peaks and the impacts on optical performance. For example, Parks and Evans demonstrated post-polishing of diamond-turned optics using conformal sub-aperture laps [168]. Pseudo-random post-polishing to mitigate MSF errors, preferably without changing the surface form, has been investigated [166,169], and a proprietary, full-aperture conformal polishing technique has been shown to reduce the amplitude of deterministic MSF surface errors [170]. Shahinian *et al*. have demonstrated a reduction of MSF errors using a custom, fiber-based finishing tool, optimized to be stiff at short-length scales but compliant at longer-length scales [113]. Recent work on laser polishing may also find application in MSF error mitigation [125].

7. METROLOGY OF FREEFORM OPTICS

Here, we will limit the discussion to techniques that have been either commercialized or demonstrated even in the laboratory's limited form. Quantifying the metrology of complex shaped objects has unique challenges. The freeform departure from the best matching sphere impacts the measurement's difficulty, which does not account for either the power term or the surfaces being concave or convex. Complexity apart, manufacturers have a wish list for freeform metrology [171]. They include a height resolution better than 1 nm and a lateral resolution allowing several hundred measurements across the aperture. Also, measures should be traceable to the international length standard. The metrology should have a verified uncertainty in measurement better than 1/10th of the applied wavelength across the whole field [172]. The instruments may provide measurements for a wide range of surfaces and their measurands of interest.

In light of concurrent engineering, the design process must consider the stages at which measurements are required and what instrument will meet requirements [56. Monitoring all stages of the freeform manufacturing process provides valuable feedback data [37]. Emerging freeform metrology solutions may offer in-situ or on-machine measurements that eliminate sample positioning errors but may suffer from a bias typical of machining errors, which may go undetected. They also need to consider environmental stability as these typically operate in harsher environments. Most importantly, the measurement and data-processing time

keep the machine idle and affect costs. Thus, decoupling the metrology from the manufacturing system currently offers a superior solution. Metrologies to consider for all processes are form and finish measurements, as well as MSFs. Grinding requires sub-surface damage assessment, specifically how deep the damage is. Finding suitable metrology is preferable to employing a "one-instrument-measures-all" solution.

Full-field Interferometry. Interferometry can provide form and MSF measurements with a repeatability of a few nanometers, assuming (a) a stable measurement environment, (b) the maximum unambiguous optical path difference is linked to the wavelength, and the maximum slope is measurable, (c) there is a reference surface, and (d) surface roughness is considered.

Commercial Fizeau interferometers have been demonstrated to reliably measure both form and MSF in challenging environments, while maintaining high lateral resolution (e.g., 250 cycles/aperture with an instrument transfer function >50%) [173]. However, as freeform surface departures may range from mild to extreme, regular reference surfaces may produce a fringe pattern that cannot be resolved by the interferometer's camera, thus requiring optical nulls. Computer Generated Holograms (CGHs) are diffractive optical elements that produce reference wavefronts as optical nulls [174]. Modeling these wavefront errors [175] is essential for accurate measurements. Other sources of errors include any mismatch in wavefront magnifications [176] or misalignments of the sample or the CGH [177]. When uncorrected, these errors can lead to measurement errors on the order of several tens of nanometers [177]. The moderately high costs of CGHs are justified in some high-volume applications.

Alternatives to CGHs are dynamic adjustable optical nulls that enable reducing cost. A deformable mirror-based null was first demonstrated in 2014 [178]. The stability of the modulator, the dynamic range, and its calibration are of consideration. Alternative adjustable nulls based on spatial light modulators reach a higher dynamic range [179,180].

Subaperture stitching can provide significant extensions to an interferometer's capability enabling the measurement of optical parts with higher slopes and higher resolution [181]. An alternative to full-aperture nulls is sub-aperture quasi-nulls [182]. In this approach, each patch is evaluated against a best-fit toroid. Adjusting each patch to the interferometer requires high-precision and flexible multiaxial kinematics and sophisticated stitching techniques.

White light interferometry (WLI) is null-free metrology that provides accurate measurements in the MSF range. If the measurement time permits, WLI is a common choice for MSF structure measurements in off-axis configurations. Deck reported a global uncertainty of <100 pm for surfaces up to 450 mm in size with aspheric departures up to 2 μm/mm [183]. WLI can routinely achieve sub-angstrom precision.

Retrace errors are present in interferometers [184]. It is possible to eliminate them using relative pupil positions [185] or measurements of tilted off-axis flats [186]. In WLI systems, a similar effect is also present: for tilted or curved surfaces, the different wavelengths travel at slightly different paths [187]. Hovis showed that these errors are around 2 nm [188], which is too high for accurate wavefront stitching. Hovis further showed using an aberration-based model that higher-order comatic terms are required for tilt angles >1.5°.

Other Coherent Measurement Techniques. Other coherent measurement techniques do not require optical nulls. An example is the Tilted Wave Interferometer (TWI) [189], which employs multiple point sources that illuminate a sample region from different directions. Only one of the point sources creates a fringe pattern equivalent to the departure from the best-fit sphere in this system. The TWI measurement time is in the order of a few seconds, and the deviation from the best fit sphere on the order of several hundreds of micrometers. TWI's challenge is converting the optical path difference to a height map, which is realized by a four-dimensional look-up-table. We note that digital holography techniques may find applications in freeform optics metrology [190].

Another coherent measurement technique is phase retrieval (PRT), which has high environmental stability. A specific method, transverse translation-diverse phase retrieval (TTDPR), has been applied to optical components' metrology, including freeform [191,192]. TTDPR illuminates a sub-aperture and captures a series of diffraction images as the sub-aperture translates over the optics. The wavefront aberration and the corresponding surface sag error are reconstructed from the diffraction images using a nonlinear optimization algorithm.

Freeform metrology also includes slope measuring systems. Lateral shearing interferometry is robust but cannot measure spatial surface wavelengths equal to the shear period or a fraction. Swain *et al.* reported a slope measuring system based on spatially dithered distributions of binary pixels to synthesize a far-field amplitude mask [193]. The approach overcomes the low spatial resolution and limited dynamic range of Shack–Hartman wavefront sensors (SHWS). Cost-effective SHWS have nevertheless been applied to freeform metrology using sub-aperture stitching [194]. Also, a differential Shack–Hartman technique for measuring local curvature of parts was demonstrated [195].

Phase Measuring Deflectometry. Knauer *et al.* reported phase measuring deflectometry (PMD) to measure specular objects [196]. Since the original invention in 1999, deflectometry has been gaining popularity. It provides a null–free full-frame metrology solution with short measurement times that plays out its strength for large and complex freeform optics [197]. As pointed out by Blalock [198], PMD can "measure MSF errors on freeform parts orders of magnitude faster than traditional tactile metrology tools."

PMD systems are highly sensitive slope measuring systems and have high repeatability. High surface slopes and sub-nanometer repeatability for environment instability and noise (i.e., 0.6 nm RMS) with an overall slope measurement accuracy near ∼100 nrad have been demonstrated [199]. The PMD is less sensitive to sample misalignments. Davies *et al.* used PMD to measure five-degree of freedom misalignments in segmented telescope mirrors [200]. The PMD can be combined with multi-frequency techniques to obtain measurements beyond the MTF limit [201]. A critical element in PMD systems is its numerical reconstruction algorithm. It is necessary to develop in-house software because commercial packages do not keep up with the latest developments that achieve high precision measurements. As in techniques measuring slopes or curvature, surface shapes are computed using numerical integration with Zonal [202], Modal [203], or Hybrid techniques [204]. Self-calibration and numerical integration may be combined [205].

We note that PMD is extremely sensitive to out-of-plane deformations and is less sensitive to systematic errors in comparative measurements. Systematic errors are calibrated down to the 20 nm level in the Zernike coefficients using a reference artifact accurately measurable with a slower metrology instrument [206].

Coordinate Measuring Machines, Point Probes, and Atomic Force Microscopy. Coordinate measuring machines (CMMs) provide point-wise measurements over large measurement volumes and handle steep surface slopes. The measurements are independent of the sample alignment for contact probes, which provides actual coma-measurements machined on the surface. As a well-established technique, the metrology community has a widely accepted terminology for the errors [207,208].

Challenges with CMM-based techniques include large measurement times (e.g., centimeter-class aspheres require 15 min), the normal incidence condition, and systematic errors. The measurement along the normal requires additional tilt axes or adapted coordinate measuring machines working in cylindrical or spherical coordinates. These limitations diminish their value in industrial practice.

Despite these challenges, commercial CMMs provide remarkably high accuracy. With atomic force probe technology in the stylus and HeNe laser-based interferometric XYZ axis positioning, one approach achieves an uncertainty of 100 nm and a repeatability of 50 nm [209]. A tactile probe combined with advanced cameras resolves 7.5 nm and achieves an uncertainty of 250 nm. Another approach achieves 30 nm uncertainty for a 500 mm diameter part with nanometer resolution, all reported by Nouira *et al.* [210]. Optical probes with 0.1 nm resolution are also available, but the position accuracy remains near 1 μm [211]. CMMs can measure freeforms with an estimated ±50 nm uncertainty based on aspheres' measurements.

Other solutions are on-machine measurement systems, where a single-point probe replaces the tool. This configuration may provide a false sense of accuracy because it cannot measure systematic errors. A circumvention is to measure on a separate CMM. Another circumvention is to manufacture the part with independent axes (e.g., using two linear axes to manufacture and a rotary axis for metrology).

An example of using a diamond turning machine as a CMM has been reported [212]. Noste used a Moore Nanotech 100UMM for measuring a 400 mm part by mounting the component on the C-carriage and a chromatic confocal probe on the B-carriage. A critical step was modeling machine errors, as well as volumetric errors [213]. Then, thermal errors dominate. The thermal drifts and some remaining carriage motion errors were compensated down to 20–30 nm.

One advantage of CMMs is incorporating a wide range of single-point probes, confocal probes being the most popular. Some commercial probes' dynamic range spans 1,000–50,000, with axial resolutions between 2 and 79 nm [214]. Measurements span 100 μm to 38.5 mm. Chromatic confocal probes offer a measurement range between 15 μm and 24 mm, with a noise level between 7 and 800 nm, and a dynamic range between 13,000 and 30,000 [215]. Low-coherence interferometric probes leverage coherence gating [216]. Optical CMMs with scans normal to the surface to meet high dynamic ranges leverages both low-coherence gating probes and chromatic probes to achieve ±150 nm uncertainty [217]. Operating in telecentric mode overcomes critical alignment issues [218]. Also commercialized are several interferometric probes with an axial resolution 1–5 nm, measurement ranges between 4 and 12 microns, and dynamic ranges between 3,000 and 4,000,000 [219].

Multi-wavelength interferometry (MWI) probes have been successfully implemented [212]. There is an emerging field in the area of ultra-high dynamic range MWI probes. Falaggis *et al.* reported several probe designs that operate over several tens of mm with a dynamic range >2, 000, 000 [220,221] at high temporal bandwidths. Specialized probes are also of research interest [222]. Most optical probes have a probing beam with a spot size between 1.2 and 25 μm, which may be enough for form and MSF measurements, but not for roughness measurements.

At the extreme limits of CMMs, there is atomic force microscopy [223]. One may compute surface properties from the measured 3D structure, such as surface roughness, autocorrelation, and the structure function [224]. A limitation is an allowance for smaller parts.

Surface Scattering Techniques. These techniques are part of another family of metrology approaches that provide unique solutions to surface characterization by analyzing scattered light from surface topography (including roughness), contamination, bulk index fluctuations, and sub-surface defects [225]. Surface scattering techniques (SSTs) yield surface characteristics without knowing the phase of the measured signal. The bidirectional scatter distribution function (BSDF) represents the scattering properties [226,227]. The BSDF is related to the power spectral density (PSD) of the surface perturbation [228], from which RMS roughness, RMS slope, and average surface wavelength are computed [229]. Total integrated scatter (TIS) measurements also yield RMS values with attention to measurement bandwidth and incidence angle. Although BSDF measurements provide more information, TIS measurements are the most cost-effective [229,230].

8. OUTLOOK

In the context of the themes discussed in this paper, we now identify both near and long-term future directions. Concurrent engineering requires optical and optomechanical designs to be created, not sequentially but in parallel with other critical aspects of system engineering, to minimize time to market and expensive redesign cycles. Here, the future holds unambiguous transmission of design intent via an expanding suite of ISO standards [231]. Developing work connecting functional performance and MSFs needs to be matched by specification methods. Next-generation CAD/CAM packages are necessary to generate tool paths for all manufacturing process platforms.

Another theme is developing a roadmap. Both current capabilities and gaps in these capabilities for freeform optics are identified, thus providing an opportunity to guide future advancements and maximize impact. Creating a roadmap also allows the emergence of a broader research and development community, spanning academia, industry, and national laboratories. In this context, industry involvement is especially important since, as our previous discussion demonstrates, there are broad pre-competitive research fields for which a common approach is likely most beneficial.

In the design space, the interest in all-reflective multi-mirrors unobscured freeform systems continues to grow as methods have been established for choosing the best folding geometries in terms of the ability to correct for optical aberrations [59]; whether for a camera, a telescope, a viewfinder, or extreme ultra-violet lithography (EUVL) projection optics. In addition, freeform optics offer the means to create more compact imager solutions by a factor of about $3X$ in volume [32]. CubeSats and drones are enabled. A technology that enables significantly more compact and well-corrected geometries will be embraced broadly across applications, assuming that materials and costs cooperate.

For spectrometers, whose application domains range from space optics to biomedical research, freeform optics is poised to ensure compact form factors with up to a five-time reduction in volume, provided fixed specifications. For a given volume, freeform expands the possibilities for spectral bandwidth and field of view [30].

Small refractive freeform optics targeted at specific optical functions include field lenses for unique distortion mappings and Alvarez lenses for multi-focus capability [93]. Alvarez-like lenses may achieve more general dynamic functions [232]. We anticipate their imminent permeation into the consumer market.

For more than 400 years, "subtractive" manufacturing has prevailed, including grinding, finishing, polishing, turning, and milling [233]. The challenge in these techniques includes building knowledge of how materials behave, especially as manufacturing pushes increasingly higher feeds and speeds. Also, precision manufacturing may create parts where fiducials and built-in kinematic fixtures will enable the broader adoption of snap-together assemblies to meet stringent specifications of visible and ultraviolet freeform systems [234].

Additive manufacturing currently targets both reflective and refractive small-size optics, but developments are at early stages. Overall, optical components have been mostly produced by a number of polymer additive manufacturing processes [235,236]. We also see recent advances in developing optics for the visible spectrum; an example is high-quality optical freeform surfaces manufactured by two-photon polymerization [237]. Additive manufacturing of ceramics (e.g., oxides, SiC) is also in its early stages [238]. Metal additive manufacturing, combined with topological optimization, offers the prospect of producing light, stiff, and athermal structures in Invar [239]. This may subsequently be plated and finished.

One challenge in the context of specific materials is to overcome 3D manufacturing limitations in terms of pixel size and means of adding materials. For example, the 3D manufacturing of glasses/oxides, or materials with high melting points such as SiC, provides particular challenges given the high temperatures involved. Spanning reflective and refractive, incorporating diffractive elements onto curved [240,241], and freeform surfaces is a challenging area accounting for the spatially varying curvature [242]. Molding and replicating point toward broader mass manufacturing, as discussed previously.

Extreme ultraviolet lithography optics provide proof that difficult, off-axis aspheric surfaces can be produced with ~single nm RMS form errors on apertures of hundreds of mm [70]. The next-generation EUVL projection optics demand the use of freeforms [243]. While off-axis aspheres do not meet the rigorous definition of freeform surfaces, they inspire that there is room to develop freeform optics with tolerances typically associated with very short wavelengths. The authors also expect that artificial intelligence and machine learning algorithms and methods will significantly contribute to the evolution of freeform optical systems, as they have already in EUVL and other fields [244].

In metrology, high-accuracy flexible form measurement remains today's challenge. Efforts across extensive collaborations in round-robin experiments are underway to advance the metrology roadmap and complete a gap analysis. Metrology of surface shapes will remain in demand as a critical enabler for convergence to manufacturing chain specifications. Final assembly quality-certification requires system-level metrology. Cost demands optimization of start-up and usage times.

Furthermore, the issue of MSF errors continues to create challenges in metrology and manufacturing. Although we have identified approaches toward mitigating MSFs, the mitigation may occur at the freeform component or system level. Therefore, performance assessment at the system level is practically essential, and a roadmap must include capabilities and gaps at the system level.

We may also assess a nominal metrology cost. The measurement time and complexity of the metrology solution are directly related to the manufactured freeform optics costs. Sophisticated solutions are affordable for the EUVL industry. EUVL requires small volumes of outstanding freeform optics to provide imaging performance for integrated circuit generations below the 11 nm node. High volume applications, such as cell phone camera lenses and fiber optic connectors, will use statistical process control and sampling to achieve adequate yield from high-volume production. A current challenge is for low-volume, moderate-uncertainty metrology, where the economics of flexible solutions conflict with the desired tolerances. Here we define a term that we refer to as *metrology complexity* that serves as a measure of a metrology problem's complexity and solution. Metrology complexity increases with (1) the aperture, (2) the sag departure, (3) the power of the part under test, (4) the number of convex surface patches, (5) the maximum surface slope, (6) the maximum spatial frequency to be measured relative to the test wavelength, (7) the environmental stability, (8) the diffractive nature of the sample, (9) the surface roughness, and (10) the measurement speed. The final solution cost increases with (i) the metrology complexity, (ii) the measurement time, (iii) the time a company needs to establish a process, but also decreases with (iv) the manufacturing volume and (v) the manufacturing process stability.

In summary, we have found that academic, industrial, and national-lab collaboration is essential in realizing the near-term possibilities. In the context of pre-competitive research, this collaboration can and will be productive both in detailing and filling gaps in a roadmap for the broad field of freeform optics.

Funding. Industry members of the Center for Freeform Optics (https://centerfreeformoptics.org); National Science Foundation (IIP-1338877, IIP-1338898, IIP-1822026, IIP-1822049); II-VI Foundation (Block Gift Program).

Acknowledgment. There are so many people to thank, and we cannot do justice to all the contributions made in design, fabrication, and metrology. The pioneering work of James Baker and William Plummer, designing and building the first freeform lenses that made the SX-70 consumer market camera, is our inspiration. We extend our thanks to the students who provided feedback on full sections of this mini-review, specifically, Nick Takaki (Mathematical Surface Descriptions), Jonathan Papa (Design), Ezron Manco (Fabrication), Luke DeMars (MSF), and Di Xu and Romita Chaudhuri (Metrology).

Dedication. We dedicate this paper to the late Kevin P. Thompson and late Roland V. Shack. Their invention of nodal aberration theory in 1980 laid the groundwork for freeform optics design methods in imaging. Kevin was also a pillar in building the freeform optics community. In addition, a co-dedication goes to the late Stephen Jacobs and late Harvey Pollicove for their contributions to process science and engineering, and to the group at LLNL led by the late Jim Bryan and late Bob Donaldson, who pioneered applying the deterministic principle to ultra-precision manufacturing. Thank you. You are our guiding stars!

Disclosures. The authors declare no conflicts of interest.

REFERENCES

1. H. Chretien, "Anamorphotic lens system and method of making the same," U.S. patent 1,962,892 (June 12, 1934).

2. J. M. Rodgers and K. P. Thompson, "Benefits of freeform mirror surfaces in optical design," in *Proceedings of the American Society of Precision Engineering 2004 Winter Topical Meeting on Freeform Optics* (2004), pp. 73–78.
3. H. J. Birchall, "Lens of variable focal power having surfaces of involute form," U.S. patent 2,475,275 (July 5, 1949).
4. L. W. Alvarez and W. E. Humphrey, "Variable-power lens and system," U.S. patent 3,507,565 (April 21, 1970).
5. M. Peloux and L. Berthelot, "Optimization of the optical performance of variable-power and astigmatism Alvarez lenses," Appl. Opt. **53**, 6670–6681 (2014).
6. A. Wilson and H. Hua, "Design and demonstration of a vari-focal optical see-through head-mounted display using freeform Alvarez lenses," Opt. Express **27**, 15627–15637 (2019).
7. W. T. Plummer, "Unusual optics of the polaroid SX-70 Land camera," Appl. Opt. **21**, 196–208 (1982).
8. W. T. Plummer, J. G. Baker, and J. Van Tassell, "Photographic optical systems with nonrotational aspheric surfaces," Appl. Opt. **38**, 3572–3592 (1999).
9. A. Offner, "Catoptric anastigmatic afocal optical system," U.S. patent 3,674,334 (July 4, 1972).
10. L. G. Cook, "Three mirror anastigmatic optical system," U.S. patent 4,265,510 (May 5, 1981).
11. W. B. Wetherell and D. A. Womble, "All-reflective three element objective," U.S. patent 4,240,707 (December 23, 1980).
12. R. A. Buchroeder and A. S. Leonard, "Wide-field tilted-component telescope: a Leonard extended Yolo all-reflecting system," Appl. Opt. **11**, 1649–1651 (1972).
13. B. Tatian, "Aberration balancing in rotationally symmetric lenses," J. Opt. Soc. Am. **64**, 1083–1091 (1974).
14. D. Shafer, "Design with two-axis aspheric surfaces," Proc. SPIE **147**, 171–176 (1978).
15. T. Nakano and Y. Tamagawa, "Configuration of an off-axis three-mirror system focused on compactness and brightness," Appl. Opt. **44**, 776–783 (2005).
16. K. Fuerschbach, J. P. Rolland, and K. P. Thompson, "A new family of optical systems employing phi-polynomial surfaces," Opt. Express **19**, 21919–21928 (2011).
17. K. Fuerschbach, G. E. Davis, K. P. Thompson, and J. P. Rolland, "Assembly of a freeform off-axis optical system employing three phi-polynomial Zernike mirrors," Opt. Lett. **39**, 2896–2899 (2014).
18. H. Hoshi, N. Taniguchi, H. Morishima, T. Akiyama, S. Yamazaki, and A. Okuyama, "Off-axial HMD optical system consisting of aspherical surfaces without rotational symmetry," Proc. SPIE **2653**, 234–242 (1996).
19. O. Cakmakci, S. Vo, H. Foroosh, and J. P. Rolland, "Application of radial basis functions to shape description in a dual-element off-axis magnifier," Opt. Lett. **33**, 1237–1239 (2008).
20. D. Cheng, Y. Wang, C. Xu, W. Song, and G. Jin, "Design of an ultra-thin near-eye display with geometrical waveguide and freeform optics," Opt. Express **22**, 20705–20719 (2014).
21. A. Bauer and J. Rolland, "Design of a freeform electronic viewfinder coupled to aberration fields of freeform optics," Opt. Express **23**, 28141–28153 (2015).
22. P. Benítez, J. C. Miñano, D. Grabovickic, P. Zamora, M. Buljan, B. Narasimhan, and M. Nikolic, "Freeform optics for virtual reality applications," in *Optical Design and Fabrication (Freeform, IODC, OFT)*, OSA Technical Digest (Optical Society of America, 2017), paper ITu2A.1.
23. A. Bauer, M. Pesch, J. Muschaweck, F. Leupelt, and J. P. Rolland, "All-reflective electronic viewfinder enabled by freeform optics," Opt. Express **27**, 30597–30605 (2019).
24. H. Ries and J. Muschaweck, "Tailored freeform optical surfaces," J. Opt. Soc. Am. A **19**, 590–595 (2002).
25. C. Canavesi, W. J. Cassarly, and J. P. Rolland, "Target flux estimation by calculating intersections between neighboring conic reflector patches," Opt. Lett. **38**, 5012–5015 (2013).
26. S. Sorgato, R. Mohedano, J. Chaves, M. Hernández, J. Blen, D. Grabovičkić, P. Benítez, J. C. Miñano, H. Thienpont, and F. Duerr, "Compact illumination optic with three freeform surfaces for improved beam control," Opt. Express **25**, 29627–29641 (2017).
27. J. Chaves, *Introduction to Nonimaging Optics* (CRC Press, 2017).
28. M. Mirhosseini, O. S. Magaña-Loaiza, M. N. O'Sullivan, B. Rodenburg, M. Malik, M. P. J. Lavery, M. J. Padgett, D. J. Gauthier, and R. W. Boyd, "High-dimensional quantum cryptography with twisted light," New J. Phys. **17**, 033033 (2015).
29. M. Chrisp, L. Petrilli, M. Echter, and A. Smith, "Freeform surveillance telescope demonstration," in *MSS Parallel Conference, MSS by BRTRC Federal Solutions under contract (Ed)* (DTIC, 2019), pp. 2769–2775.
30. J. Reimers, A. Bauer, K. P. Thompson, and J. P. Rolland, "Freeform spectrometer enabling increased compactness," Light Sci. Appl. **6**, e17026 (2017).
31. R. Geyl, E. Ruch, R. Bourgois, R. Mercier-Ythier, H. Leplan, and F. Riguet, "Freeform optics design, fabrication and testing technologies for space applications," Proc. SPIE **11180**, 111800P (2019).
32. E. M. Schiesser, A. Bauer, and J. P. Rolland, "Effect of freeform surfaces on the volume and performance of unobscured three mirror imagers in comparison with off-axis rotationally symmetric polynomials," Opt. Express **27**, 21750–21765 (2019).
33. S. Cui, N. P. Lyons, L. R. Diaz, R. Ketchum, K.-J. Kim, H.-C. Yuan, M. Frasier, W. Pan, and R. A. Norwood, "Silicone optical elements for cost-effective freeform solar concentration," Opt. Express **27**, A572–A580 (2019).
34. L. Wei, Y. Li, J. Jing, L. Feng, and J. Zhou, "Design and fabrication of a compact off-axis see-through head-mounted display using a freeform surface," Opt. Express **26**, 8550–8565 (2018).
35. Y. Liu, Y. Li, and Z. Cao, "Design method of off-axis extreme ultraviolet lithographic objective system with a direct tilt process," Opt. Eng. **54**, 075102 (2015).
36. C. Yoon, A. Bauer, D. Xu, C. Dorrer, and J. P. Rolland, "Absolute linear-in-k spectrometer designs enabled by freeform optics," Opt. Express **27**, 34593–34602 (2019).
37. F. Z. Fang, X. D. Zhang, A. Weckenmann, G. X. Zhang, and C. Evans, "Manufacturing and measurement of freeform optics," CIRP Ann. **62**, 823–846 (2013).
38. O. Cakmakci, B. Moore, H. Foroosh, and J. P. Rolland, "Optimal local shape description for rotationally non-symmetric optical surfaces design and analysis," Opt. Express **16**, 1583–1589 (2008).
39. P. Jester, C. Menke, and K. Urban, "B-spline representation of optical surfaces and its accuracy in a ray trace algorithm," Appl. Opt. **50**, 822–828 (2011).
40. P. Jester, C. Menke, and K. Urban, "Wavelet methods for the representation, analysis and simulation of optical surfaces," IMA J. Appl. Math. **77**, 495–515 (2012).
41. M. Chrisp, "Method of and system for optimizing NURBs surfaces for an imaging system," U.S. patent 10,437,943 B2 (October 8, 2019).
42. I. Kaya and J. P. Rolland, "Hybrid RBF and local φ-polynomial freeform surfaces," Adv. Opt. Technol. **2**, 81–88 (2013).
43. F. Zernike, "Beugungstheorie des Schneidenver-Fahrens und seiner verbesserten form, der phasenkontrastmethode," Physica **1**, 689–704 (1934).
44. G. W. Forbes, "Characterizing the shape of freeform optics," Opt. Express **20**, 2483–2499 (2012).
45. N. Takaki, A. Bauer, and J. P. Rolland, "On-the-fly surface manufacturability constraints for freeform optical design enabled by orthogonal polynomials," Opt. Express **27**, 6129–6146 (2019).
46. Q. Meng, H. Wang, W. Liang, Z. Yan, and B. Wang, "Design of off-axis three-mirror systems with ultrawide field of view based on an expansion process of surface freeform and field of view," Appl. Opt. **58**, 609–615 (2019).
47. J. Ye, L. Chen, X. Li, Q. Yuan, and Z. Gao, "Review of optical freeform surface representation technique and its application," Opt. Eng. **56**, 110901 (2017).
48. "Part 19: general description of surfaces and components," ISO 10110-19 (2015).
49. J. Kumler, "Designing and specifying aspheres for manufacturability," Proc. SPIE **5874**, 58740C (2005).
50. N. Takaki, A. Bauer, and J. P. Rolland, "Degeneracy in freeform surfaces described with orthogonal polynomials," Appl. Opt. **57**, 10348–10354 (2018).
51. N. Takaki, J. C. Papa, A. Bauer, and J. P. Rolland, "Off-axis conics as base surfaces for freeform optics enable null testability," Opt. Express **28**, 10859–10872 (2020).
52. P. Yoder and D. Vukobratovich, *Opto-Mechanical Systems Design* (CRC Press, 2015).
53. K. J. Kasunic, *Optomechanical Systems Engineering* (Wiley, 2015).
54. S. Kalpakjian and S. Schmid, *Manufacturing processes for Engineering Materials* (Pearson, 2007).

55. N. W. Horvath and M. A. Davies, "Concurrent engineering of a next-generation freeform telescope: mechanical design and manufacture," Proc. SPIE **10998**, 109980X (2019).
56. K. Venditti, C. Evans, K. Falaggis, A. Blum, R. Chaudhuri, J. Goodsell, and J. P. Rolland, "Design for metrology for freeform optics manufacturing," Procedia CIRP **84**, 169–172 (2019).
57. N. W. Horvath, I. W. Barron, J. D. Owen, B. S. Dutterer, E. Schiesser, A. Bauer, J. P. Rolland, and M. A. Davies, "Optomechanical design and fabrication of a snap together freeform TMA telescope," in *Proc. ASPE 32nd Annual Meeting* (2017), pp. 133–138.
58. J. Lambropoulos, "Twyman effects in thin curved optics," Proc. SPIE **10448**, 104480V (2017).
59. A. Bauer, E. M. Schiesser, and J. P. Rolland, "Starting geometry creation and design method for freeform optics," Nat. Commun. **9**, 1756 (2018).
60. H. H. Hopkins, *Wave Theory of Aberrations* (Oxford/Clarendon, 1950).
61. R. V. Shack and K. Thompson, "Influence of alignment errors of a telescope system on its aberration field," Proc. SPIE **251**, 146–153 (1980).
62. R. A. Buchroeder, "Tilted component optical systems," Ph.D. dissertation (University of Arizona, 1976).
63. K. P. Thompson, T. Schmid, O. Cakmakci, and J. P. Rolland, "Real-ray-based method for locating individual surface aberration field centers in imaging optical systems without rotational symmetry," J. Opt. Soc. Am. A **26**, 1503–1517 (2009).
64. J. C. Papa and J. P. Rolland, "Calculation of sigma vectors," Appl. Opt., submitted for publication.
65. K. P. Thompson, "Description of the third-order optical aberrations of near-circular pupil optical systems without symmetry," J. Opt. Soc. Am. A **22**, 1389–1401 (2005).
66. K. P. Thompson, "Multinodal fifth-order optical aberrations of optical systems without rotational symmetry: spherical aberration," J. Opt. Soc. Am. A **26**, 1090–1100 (2009).
67. K. P. Thompson, "Multinodal fifth-order optical aberrations of optical systems without rotational symmetry: the comatic aberrations," J. Opt. Soc. Am. A **27**, 1490–1504 (2010).
68. K. P. Thompson, "Multinodal fifth-order optical aberrations of optical systems without rotational symmetry: the astigmatic aberrations," J. Opt. Soc. Am. A **28**, 821–836 (2011).
69. K. Fuerschbach, J. P. Rolland, and K. P. Thompson, "Theory of aberration fields for general optical systems with freeform surfaces," Opt. Express **22**, 26585–26606 (2014).
70. C. Menke and G. W. Forbes, "Optical design with orthogonal representations of rotationally symmetric and freeform aspheres," Adv. Opt. Technol. **2**, 97–109 (2013).
71. J. Sasian, "How to approach the design of bilateral symmetric optical systems," Opt. Eng. **33**, 2045–2061 (1994).
72. D. S. Goodman, "General principles of geometric optics," in *Handbook of Optics* (McGraw-Hill, 1995), pp. 1115–20.
73. B. D. Stone and G. W. Forbes, "Foundations of second-order layout for asymmetric systems," J. Opt. Soc. Am. A **9**, 2067–2082 (1992).
74. D. Reshidko and J. Sasian, "Method for the design of nonaxially symmetric optical systems using freeform surfaces," Opt. Eng. **57**, 101704 (2018).
75. J. M. Sasián, "Method of confocal mirror design," Opt. Eng. **58**, 015101 (2019).
76. J. C. Papa, J. M. Howard, and J. P. Rolland, "Starting point designs for freeform four-mirror systems," Opt. Eng. **57**, 101705 (2018).
77. J. C. Papa, J. M. Howard, and J. P. Rolland, "Automatic solution space exploration for freeform optical design," in *Optical Design and Fabrication (Freeform, OFT)*, OSA Technical Digest (Optical Society of America, 2019), paper FM4B.1.
78. P. Benítez, R. Mohedano, and J. C. Miñano, "Design in 3D geometry with the simultaneous multiple surface design method of nonimaging optics," Proc. SPIE **3781**, 11–21 (1999).
79. J. C. Miñano, P. Benítez, and B. Narasimhan, "Freeform aplanatic systems as a limiting case of SMS," Opt. Express **24**, 13173–13178 (2016).
80. T. Yang, G.-F. Jin, and J. Zhu, "Automated design of freeform imaging systems," Light Sci. Appl. **6**, e17081 (2017).
81. J. A. S. Hocken, B. Borchardt, J. Lazar, C. Reeve, P. Stein, and R. Young, "Three dimensional metrology," CIRP Ann. **26**, 403–408 (1977).
82. C. J. Evans, *Precision Engineering: An Evolutionary View* (Cranfield, 1989).
83. H. F. Fernandez-Moran, "A new microtome with a diamond knife," Mikroskopie **12**, 81–88 (1957).
84. C. J. Evans, "Precision engineering: an evolutionary perspective," Philos. Trans. R. Soc. London, Ser. A **370**, 3835–3851 (2012).
85. R. J. Benjamin, "Diamond turning at a large optical manufacturer," Opt. Eng. **17**, 574–577 (1978).
86. T. Saito, "Diamond turning of optics," Opt. Eng. **15**, 431–434 (1976).
87. J. B. Bryan, "Design and construction of an 84 inch diamond turning machine," Precis. Eng. **1**, 13–17 (1979).
88. R. Donaldson and S. Patterson, "Design and construction of a large, vertical axis diamond turning machine," Proc. SPIE **0433**, 62–67 (1983).
89. S. R. Patterson and E. B. Magrab, "Design and testing of a fast tool servo for diamond turning," Precis. Eng. **7**, 123–128 (1985).
90. L. Zhu, Z. Li, F. Fang, S. Huang, and X. Zhang, "Review on fast tool servo machining of optical freeform surfaces," Int. J. Adv. Manuf. Technol. **95**, 2071–2092 (2018).
91. J. Yang and Y. Altintas, "Generalized kinematics of five-axis serial machines with non-singular tool path generation," Int. J. Mach. Tools Manuf. **75**, 119–132 (2013).
92. J. D. Owen, J. A. Shultz, T. J. Suleski, and M. A. Davies, "Error correction methodology for ultra-precision three-axis milling of freeform optics," CIRP Ann. **66**, 97–100 (2017).
93. P. J. Smilie, T. J. Suleski, B. Dutterer, J. L. Lineberger, and M. A. Davies, "Design and characterization of an infrared Alvarez lens," Opt. Eng. **51**, 013006 (2012).
94. J. Mayr, J. Jedrzejewski, E. Uhlmann, M. A. Donmez, W. Knapp, F. Härtig, K. Wendt, T. Moriwaki, P. Shore, R. Schmitt, C. Brecher, T. Würz, and K. Wegener, "Thermal issues in machine tools," CIRP Ann. **61**, 771–796 (2012).
95. I. Saunders, L. Ploeg, M. Dorrepaal, and B. van Venrooij, "Fabrication and metrology of freeform aluminum mirrors for the SCUBA-2 instrument," Proc. SPIE **5869**, 0501–0512 (2005).
96. J. H. M. Beier, T. Peschel, C. Damm, A. Gebhardt, S. Scheiding, D. Stumpf, U. D. Zeitner, S. Risse, R. Eberhardt, and A. Tünnermann, "Development, fabrication, and testing of an anamorphic imaging snap-together freeform telescope," Appl. Opt. **54**, 3530–3542 (2015).
97. J. D. Owen, M. A. Davies, D. Schmidt, and E. H. Urruti, "On the ultra-precision diamond machining of chalcogenide glass," CIRP Ann. **64**, 113–116 (2015).
98. Z. Li, X. Liu, F. Fang, X. Zhang, Z. Zeng, L. Zhu, and N. Yan, "Integrated manufacture of a freeform off-axis multi-reflective imaging system without optical alignment," Opt. Express **26**, 7625–7637 (2018).
99. J. R. Troutman, D. L. Barnhardt, J. A. Shultz, J. D. Owen, S. DeFisher, M. A. Davies, and T. J. Suleski, "Machining and metrology of a chalcogenide glass freeform lens pair," Procedia Manuf. **5**, 669–683 (2016).
100. J. D. Owen, J. R. Troutman, T. A. Harriman, A. Zare, Y. Q. Wang, D. A. Lucca, and M. A. Davies, "The mechanics of milling of germanium for IR applications," CIRP Ann. **65**, 109–112 (2016).
101. J. C. Lambropoulos, S. D. Jacobs, and J. Ruckman, "Material removal mechanisms from grinding to polishing," Ceram. Trans. **102**, 113–128 (1999).
102. R. A. Jones, "Optimization of computer controlled polishing," Appl. Opt. **16**, 218–224 (1977).
103. C. Jiao, S. Li, and X. Xie, "Algorithm for ion beam figuring of low-gradient mirrors," Appl. Opt. **48**, 4090–4096 (2009).
104. D. D. Walker, G. Yu, H. Li, W. Messelink, R. Evans, and A. Beaucamp, "Edges in CNC polishing: from mirror-segments towards semiconductors, paper 1: edges on processing the global surface," Opt. Express **20**, 19787–19798 (2012).
105. O. Faehnle, C. Reynolds, G. Yu, and D. Walker, "Machine acceleration effects on computer-controlled polishing," in *Optical Design and Fabrication (Freeform, IODC, OFT), OSA Technical Digest* (Optical Society of America, 2017), paper OM4B.1.
106. J. C. Lambropoulos, S. Salzman, T. R. Smith, J. Xu, M. Pomerantz, M. P. Shanmugam, M. A. Davies, L. L. Taylor, and J. Qiao, "Subsurface damage (SSD) assessment in ground silicon carbide (SiC)," in *Optical Design and Fabrication (Freeform, IODC, OFT), OSA Technical Digest* (Optical Society of America, 2017), paper OM3B.5.
107. S. R. Arrasmith, S. D. Jacobs, J. C. Lambropoulos, A. Maltsev, D. Golini, and W. I. Kordonski, "Use of magnetorheological finishing (MRF) to relieve residual stress and subsurface damage on lapped semiconductor silicon wafers," Proc. SPIE **4451**, 285–294 (2001).

108. J. C. Lambropoulos, T. Fang, P. D. Funkenbusch, S. D. Jacobs, M. J. Cumbo, and D. Golini, "Surface microroughness of optical glasses under deterministic microgrinding," Appl. Opt. **35**, 4448–4462 (1996).
109. J. C. Lambropoulos, S. Xu, T. Fang, and D. Golini, "Twyman effect mechanics in grinding and microgrinding," Appl. Opt. **35**, 5704–5713 (1996).
110. S. N. Shafrir, J. C. Lambropoulos, and S. D. Jacobs, "Subsurface damage and microstructure development in precision micro-ground hard ceramics using magnetorheological finishing spots," Appl. Opt. **46**, 5500–5515 (2007).
111. S. Salzman, H. J. Romanofsky, L. J. Giannechini, S. D. Jacobs, and J. C. Lambropoulos, "Magnetorheological finishing of chemical-vapor deposited zinc sulfide via chemically and mechanically modified fluids," Appl. Opt. **55**, 1481–1489 (2016).
112. P. Shanmugam, "Fundamentals of material removal in silicon carbide for freeform optics," Ph.D. dissertation (University of North Carolina at Charlotte, 2019).
113. H. Shahinian, M. Hassan, H. Cherukuri, and B. A. Mullany, "Fiber-based tools: material removal and mid-spatial frequency error reduction," Appl. Opt. **56**, 8266–8274 (2017).
114. T. Suratwala, *Materials Science and Technology of Optical Fabrication* (Wiley, 2018).
115. F. W. Preston, "The theory and design of plate glass polishing machines," J. Soc. Glass Technol. **11**, 214–256 (1927).
116. D. Mohring, M. Bechtold, and E. Fess, "Finishing of optical materials with bound and loose abrasives utilizing the ultraform 5-axis computer controlled system," in *Frontiers in Optics*, OSA Technical Digest (CD) (Optical Society of America, 2006), paper OFTuD3.
117. C. Bouvier, S. Gracewski, and S. Burns, "Contact mechanics models and algorithms for dome polishing with ultraform finishing (UFF)," Proc. SPIE **6545**, 65450R (2007).
118. D. D. Walker, G. Yu, H. Li, B. W. Myer, A. T. Beaucamp, Y. Namba, and L. Wu, "Title advances in optical fabrication for astronomy," Mon. Not. R. Astron. Soc. **485**, 2071–2082 (2019).
119. S. M. Booij, O. W. Fähnle, and J. J. Braat, "Shaping with fluid jet polishing by footprint optimization," Appl. Opt. **43**, 67–69 (2004).
120. D. Harris, "History of magnetorheological finishing," Proc. SPIE **8016**, 80160N (2011).
121. W. Messner, "Optical fabrication: magnetorheological finishing is pushed to new extremes," in LaserFocusWorld**56**(1), (2020).
122. W. I. Kordonski, A. B. Shorey, and M. Tricard, "Magnetorheological jet finishing technology," J. Fluids Eng. **128**, 20–26 (2006).
123. D. Schaefer, "Basics of ion beam figuring and challenges for real optics treatment," Proc. SPIE **10829**, 1082907 (2018).
124. J. R. Castelli, M. Morantz, and P. Shore, "Rapid optical surface figuring using reactive atom plasma," J. Precision Eng. **36**, 467–476 (2012).
125. L. L. Taylor, J. Xu, M. Pomerantz, T. R. Smith, J. C. Lambropoulos, and J. Qiao, "Femtosecond laser polishing of germanium [invited]," Opt. Mater. Express **9**, 4165–4177 (2019).
126. L. L. Taylor, J. Qiao, and J. Qiao, "Optimization of femtosecond laser processing of Silicon via numerical modeling," Opt. Mater. Express **6**, 2745–2758 (2016).
127. S. Bäumer, *Handbook of Plastic Optics*, 2nd ed. (Wiley, 2011).
128. L. Zhang, G. Liu, X. Zhao, O. Dambon, F. Klocke, and A. Yi, "Precision molding of optics: a review of its development and applications," Proc. SPIE **9949**, 994906 (2016).
129. D. Gurganus, S. Novak, A. Symmons, and M. Davies, "Process evaluation and optimization for freeform precision glass molding," Proc. SPIE **11487**, 1148710 (2020).
130. D. Aikens, A. Roussel, and M. Bray, "Derivation of preliminary specifications for transmitted wavefront and surface roughness for large optics used in inertial confinement fusion," Proc. SPIE **2633**, 350–360 (1995).
131. J. Filhaber, "Large optics: mid-spatial-frequency errors: the hidden culprit of poor optical performance," in *LaserFocusWorld* (2013).
132. J. M. Tamkin, W. J. Dallas, and T. D. Milster, "Theory of point-spread function artifacts due to structured mid-spatial frequency surface errors," Appl. Opt. **49**, 4814–4824 (2010).
133. M. Pohl and R. Börret, "Simulation of mid-spatials from the grinding process," J. Eur. Opt. Soc.—Rapid **11**, 16010 (2016).
134. A. Sohn, L. Lamonds, and K. Garrard, "Modeling of vibration in single-point diamond turning," in *Proc. ASPE 21st Annual Meeting* (2006), pp. 15–20.
135. S. Rakuff and P. Beaudet, "Thermally induced errors in diamond turning of optical structured surfaces," Opt. Eng. **46**, 103401 (2007).
136. K. Cheng, ed. *Machining Dynamics: Fundamentals, Applications, and Practices* (Springer, 2009).
137. "Optics and photonics—preparation of drawings for optical elements and systems—part 8: surface texture," ISO10110-10118:12019 (2019).
138. D. M. Aikens, J. E. DeGroote, and R. N. Youngworth, "Specification and control of mid-spatial frequency wavefront errors in optical systems," in *Frontiers in Optics/Laser Science XXIV/Plasmonics and Metamaterials/Optical Fabrication and Testing*, OSA Technical Digest (CD) (Optical Society of America, 2008) paper OTuA1.
139. J. Harvey and A. K. Thompson, "Scattering effects from residual optical fabrication errors," Proc. SPIE **2576**, 154–174 (1995).
140. G. W. Forbes, "Fitting freeform shapes with orthogonal bases," Opt. Express **21**, 19061–19081 (2013).
141. Z. Hosseinimakarem, "Mid-spatial frequency characterization and specification for freeform surfaces using Zernike polynomials," Ph.D. dissertation (University of North Carolina at Charlotte, 2017).
142. J. Stock, A. Broemel, J. Hartung, D. Ochse, and H. Gross, "Description and reimplementation of real freeform surfaces," Appl. Opt. **56**, 391–396 (2017).
143. J. Shultz, P. Smilie, B. Dutterer, M. A. Davies, and T. J. Suleski, "Experimental characterization of variable output refractive beamshapers using freeform elements," Proc. SPIE **9194**, 91940M (2014).
144. J. Stock, M. Beier, S. Merx, and H. Gross, "Simulation and analysis of optical imaging systems including real freeform components," Adv. Opt. Technol. **8**, 111–117 (2019).
145. K. Liang, G. W. Forbes, and M. A. Alonso, "Validity of the perturbation model for the propagation of MSF structure in 2D," Opt. Express **27**, 3390–3408 (2019).
146. J. M. Elson and J. M. Bennett, "Calculation of the power spectral density from surface profile data," Appl. Opt. **34**, 201–208 (1995).
147. R. E. Parks, "Specifications: figure and finish are not enough," Proc. SPIE **7071**, 70710B (2008).
148. W. J. Smith, *Modern Optical Engineering*, 3rd ed. (McGraw-Hill, 2000).
149. E. L. Church and J. M. Zavada, "Residual surface roughness of diamond-turned optics," Appl. Opt. **14**, 1788–1795 (1975).
150. J. C. Stover, "Roughness characterization of smooth machined surfaces by light scattering," Appl. Opt. **14**, 1796–1802 (1975).
151. R. Noll, "Effect of mid- and high-spatial frequencies on optical performance," Opt. Eng. **18**, 182137 (1979).
152. J. P. Marioge and S. Slansky, "Effect of figure and waviness on image quality," J. Opt. **14**, 189–198 (1983).
153. R. N. Youngworth and B. D. Stone, "Simple estimates for the effects of mid-spatial-frequency surface errors on image quality," Appl. Opt. **39**, 2198–2209 (2000).
154. J. M. Tamkin and T. D. Milster, "Effects of structured mid-spatial frequency surface errors on image performance," Appl. Opt. **49**, 6522–6536 (2010).
155. F. Tinker and K. Xin, "Correlation of mid-spatial features to image performance in aspheric mirrors," Proc. SPIE **8837**, 88370N (2013).
156. M. A. Alonso and G. W. Forbes, "Strehl ratio as the Fourier transform of a probability density of error differences," Opt. Lett. **41**, 3735–3738 (2016).
157. K. Liang and M. A. Alonso, "Understanding the effects of groove structures on the MTF," Opt. Express **25**, 18827–18841 (2017).
158. H. Aryan, K. Liang, M. A. Alonso, and T. J. Suleski, "Predictive models for the Strehl ratio of diamond-machined optics," Appl. Opt. **58**, 3272–3276 (2019).
159. "Optics and photonics—preparation of drawings for optical elements and systems—part 8: surface texture; roughness and waviness," ISO10110-10118:12010(E) (2010).
160. H. Aryan, "Performance and specification of optical components with mid-spatial frequency surface errors," Ph.D. dissertation (University of North Carolina at Charlotte, 2019).
161. L. He, C. J. Evans, and A. Davies, "Two-quadrant area structure function analysis for optical surface characterization," Opt. Express **20**, 23275–23280 (2012).
162. B. Dube, R. Cicala, A. Closz, and J. P. Rolland, "How good is your lens? Assessing performance with MTF full-field displays," Appl. Opt. **56**, 5661–5667 (2017).

163. T. Pertermann, J. Hartung, M. Beier, M. Trost, S. Schröder, S. Risse, R. Eberhardt, A. Tünnermann, and H. Gross, "Angular resolved power spectral density analysis for improving mirror manufacturing," Appl. Opt. **57**, 8692–8698 (2018).
164. H. Aryan, G. D. Boreman, and T. J. Suleski, "The minimum modulation curve as a tool for specifying optical performance: application to surfaces with mid-spatial frequency errors," Opt. Express **27**, 25551–25559 (2019).
165. H. Aryan, G. D. Boreman, and T. J. Suleski, "Simple methods for estimating the performance and specification of optical components with anisotropic mid-spatial frequency surface errors," Opt. Express **27**, 32709–32721 (2019).
166. C. R. Dunn and D. D. Walker, "Pseudo-random tool paths for CNC sub-aperture polishing and other applications," Opt. Express **16**, 18942–18949 (2008).
167. T. Hull, M. J. Riso, J. M. Barentine, and A. Magruder, "Mid-spatial frequency matters: examples of the control of the power spectral density and what that means to the performance of imaging systems," Proc. SPIE **8353**, 835329 (2012).
168. R. E. Parks and C. J. Evans, "Rapid post-polishing of diamond-turned optics," Precision Eng. **16**, 223–227 (1994).
169. X. Guo, Y. Shu, G.-H. Kim, M. Palmer, H. Choi, and D. W. Kim, "Pseudorandom orbiting stroke for freeform optics postprocessing," Opt. Eng. **58**, 092608 (2019).
170. J. DeGroote Nelson, A. Gould, C. Klinger, and M. Mandina, "Incorporating VIBE into the precision optics manufacturing process," Proc. SPIE **8126**, 812613 (2011).
171. G. Baer, J. Schindler, C. Pruss, J. Siepmann, and W. Osten, "Fast and flexible non-null testing of aspheres and free-form surfaces with the tilted-wave-interferometer," Int. J. Optomechatron. **8**, 242–250 (2014).
172. W. Bich, M. G. Cox, and P. M. Harris, "Evolution of the 'guide to the expression of uncertainty in measurement," Metrologia **43**, S161–S166 (2006).
173. D. M. Sykora and P. de Groot, "Instantaneous measurement Fizeau interferometer with high spatial resolution," Proc. SPIE **8126**, 812610 (2011).
174. S. M. Arnold, "How to test an asphere with a computer generated hologram," Proc. SPIE **1052**, 190–197 (1989).
175. V. A. Soifer, *Methods for Computer Design of Diffractive Optical Elements* (Wiley, 2001).
176. K. Creath and J. C. Wyant, "Use of computer-generated holograms in optical testing," in *Handbook of Optics*, M. Bass, ed. (McGraw-Hill Inc. 1995), Vol. **II**.
177. S. Stuerwald, "Error compensation in computer generated hologram-based form testing of aspheres," Appl. Opt. **53**, 8249–8255 (2014).
178. K. Fuerschbach, K. P. Thompson, and J. P. Rolland, "Interferometric measurement of a concave, phi-polynomial, Zernike mirror," Opt. Lett. **39**, 18–21 (2014).
179. S. Xue, S. Chen, Z. Fan, and D. Zhai, "Adaptive wavefront interferometry for unknown free-form surfaces," Opt. Express **26**, 21910–21928 (2018).
180. R. Chaudhuri, J. Papa, and J. P. Rolland, "System design of a single-shot reconfigurable null test using a spatial light modulator for freeform metrology," Opt. Lett. **44**, 2000–2003 (2019).
181. P. Murphy, G. Forbes, J. Fleig, P. Dumas, and M. Tricard, "Stitching interferometry: a flexible solution for surface metrology," Opt. Photon. News **14**, 38–43 (2003).
182. P. E. Murphy and C. Supranowitz, "Freeform testability considerations for subaperture stitching interferometry," Proc. SPIE **11175**, 111750Z (2019).
183. L. L. Deck, "High precision interferometer for measuring mid-spatial frequency departure in free form optics," Proc. SPIE **10316**, 103160N (2007).
184. Q. Hao, S. Wang, Y. Hu, H. Cheng, M. Chen, and T. Li, "Virtual interferometer calibration method of a non-null interferometer for freeform surface measurements," Appl. Opt. **55**, 9992–10001 (2016).
185. C. Huang, "Propagation errors in precision Fizeau interferometry," Appl. Opt. **32**, 7016–7021 (1993).
186. C. J. Evans and J. B. Bryan, "Compensation for errors introduced by nonzero fringe densities in phase-measuring interferometers," CIRP Ann. **42**, 577–580 (1993).
187. P. Lehmann, P. Kühnhold, and W. Xie, "Reduction of chromatic aberration influences in vertical scanning white-light interferometry," Meas. Sci. Technol. **25**, 065203 (2014).
188. C. Hovis, H. Shahinian, and C. Evans, "Observations on the effect of retrace error in scanning white light interferometry of smooth optical surfaces," in *Optical Design and Fabrication 2019 (Freeform, OFT), OSA Technical Digest* (Optical Society of America, 2019), paper OM4A-2.
189. I. Fortmeier, M. Stavridis, A. Wiegmann, M. Schulz, W. Osten, and C. Elster, "Evaluation of absolute form measurements using a tilted-wave interferometer," Opt. Express **24**, 3393–3404 (2016).
190. T. Kreis, *Handbook of Holographic Interferometry: Optical and Digital Methods* (Wiley, 2006).
191. A. M. Michalko and J. R. Fienup, "Verification of transverse translation diverse phase retrieval for concave optical metrology," Opt. Lett. **43**, 4827–4830 (2018).
192. A. Michalko and J. Fienup, "Development of a concave freeform surface measurement using transverse translation-diverse phase retrieval," Opt. Eng. **59**, 064101 (2020).
193. B. R. Swain, C. Dorrer, and J. Qiao, "High-performance optical differentiation wavefront sensing towards freeform metrology," Opt. Express **27**, 36297–36310 (2019).
194. K. K. Pant, D. R. Burada, M. Bichra, M. P. Singh, A. Ghosh, G. S. Khan, S. Sinzinger, and C. Shakher, "Subaperture stitching for measurement of freeform wavefront," Appl. Opt. **54**, 10022–10028 (2015).
195. W. Zou, K. P. Thompson, and J. P. Rolland, "Differential Shack–Hartmann curvature sensor: local principal curvature measurements," J. Opt. Soc. Am. A **25**, 2331–2337 (2008).
196. M. Knauer, J. Kaminski, and G. Hausler, "Phase measuring deflectometry: a new approach to measure specular free-form surfaces," Proc. SPIE **5457**, 365–376 (2004).
197. L. Huang, M. Idir, C. Zuo, and A. Asundi, "Review of phase measuring deflectometry," Opt. Laser Eng. **107**, 247–257 (2018).
198. T. F. Blalock, B. D. Cox, and B. Myer, "Measurement of mid-spatial frequency errors on freeform optics using deflectometry," Proc. SPIE **11056**, 110561H (2019).
199. P. Su, Y. Wang, J. H. Burge, K. Kaznatcheev, and M. Idir, "Non-null full field x-ray mirror metrology using SCOTS: a reflection deflectometry approach," Opt. Express **20**, 12393–12406 (2012).
200. A. Davies, T. Vann, C. Evans, and M. Butkiewicz, "Phase measuring deflectometry for determining 5 DOF misalignment of segmented mirrors," Proc. SPIE **10373**, 103730H (2017).
201. L. A. DeMars, A. H. Ramirez-Andrade, R. Porras-Aguilar, and K. Falaggis, "Super sensitive phase measurement deflectometry with effective fringe periods beyond the MTF limit," in *Optical Design and Fabrication (Freeform, OFT)*, OSA Technical Digest (Optical Society of America, 2019), paper OW4A.6.
202. W. H. Southwell, "Wave-front estimation from wave-front slope measurements," J. Opt. Soc. Am. **70**, 998–1006 (1980).
203. M. Aftab, J. H. Burge, G. A. Smith, L. Graves, C.-J. Oh, and D. W. Kim, "Modal data processing for high resolution deflectometry," Int. J. Precis. Eng. Manuf.-Green Tech. **6**, 255–270 (2019).
204. A. P. Fard and A. Davies, "Characterization of the interpolation bias in the analysis of deflectometry measurement data," Proc. SPIE **10749**, 107490G (2018).
205. L. Huang, J. Xue, B. Gao, C. McPherson, J. Beverage, and M. Idir, "Modal phase measuring deflectometry," Opt. Express **24**, 24649–24664 (2016).
206. W. Li, P. Huke, J. Burke, C. von Kopylow, and R. Bergmann, "Measuring deformations with deflectometry," Proc. SPIE **9203**, 92030F (2014).
207. "Geometrical product specifications (GPS)—acceptance and reverification tests for coordinate measuring machines (CMM)," ISO 10360 (2020).
208. "Geometrical product specifications (GPS)—coordinate measuring machines (CMM): technique for determining the uncertainty of measurement," ISO 15530 (2011).
209. S. Scheiding, Y. Y. Allen, A. Gebhardt, L. Li, S. Risse, R. Eberhardt, and A. Tünnermann, "Freeform manufacturing of a microoptical lens array on a steep curved substrate by use of a voice coil fast tool servo," Opt. Express **19**, 23938–23951 (2011).
210. H. Nouira, R. H. Bergmans, A. Küng, H. Piree, R. Henselmans, and H. A. M. Spaan, "Ultra-high precision CMMs and their associated tactile or/and optical scanning probes," Int. J. Metrol. Qual. Eng. **5**, 204 (2014).
211. A. Beutler, "Strategy for a flexible and noncontact measuring process for freeforms," Opt. Eng. **55**, 071206 (2016).

212. M. Conroy, R. Burton, Y. Yu, and T. Kumagi, "Recent advances in non-contact metrology, high speed measurement, steep slope measurement and correlation with stylus data," in *Proc. of Malaysian International Tribology Conference* (2015), pp. 314–315.
213. T. Noste, C. Evans, J. Miller, L. Hopper, P. L. Marasco, J. S. Sanghera, and J. N. Vizgaitis, "Concurrent engineering of a next-generation freeform telescope: metrology and test," Proc. SPIE **10998**, 109980Y (2019).
214. H. Nouira, N. El-Hayek, X. Yuan, and N. Anwer, "Characterization of the main error sources of chromatic confocal probes for dimensional measurement," Meas. Sci. Technol. **25**, 044011 (2014).
215. F. Blateyron, "Chromatic confocal microscopy," in *Optical Measurement of Surface Topography*, R. Leach, ed. (Springer, 2011).
216. J. Yao, A. Anderson, and J. P. Rolland, "Point-cloud noncontact metrology of freeform optical surfaces," Opt. Express **26**, 10242–10265 (2018).
217. S. DeFisher, G. Matthews, and J. Ross, "New advancements in freeform optical metrology," Proc. SPIE **10179**, 101790P (2017).
218. D. Xu, R. Chaudhuri, and J. P. Rolland, "Telecentric broadband objective lenses for optical coherence tomography (OCT) in the context of low uncertainty metrology of freeform optical components: from design to testing for wavefront and telecentricity," Opt. Express **27**, 6184–6200 (2019).
219. D. Li, X. Jiang, Z. Tong, and L. Blunt, "Development and application of interferometric on-machine surface measurement for ultraprecision turning process," J. Manuf. Sci. Eng. **141**, 014502 (2018).
220. K. Falaggis, D. P. Towers, and C. E. Towers, "Multiwavelength interferometry: extended range metrology," Opt. Lett. **34**, 950–952 (2009).
221. K. Falaggis and C. E. Towers, "Absolute metrology by phase and frequency modulation for multiwavelength interferometry," Opt. Lett. **36**, 2928–2930 (2011).
222. S. C. Butler, M. A. Ricci, C. Wang, Q. Wei, and J. D. Ellis, "Homodyne displacement measuring interferometer probe for optical coordinate measuring machine with tip and tilt sensitivity," Proc. SPIE **9633**, 96332E (2015).
223. R. R. L. De Oliveira, D. A. C. Albuquerque, T. G. S. Cruz, F. M. Yamaji, and F. L. Leite, "Measurement of the nanoscale roughness by atomic force microscopy: basic principles and applications," in *Atomic Force Microscopy-Imaging, Measuring and Manipulating Surfaces at The Atomic Scale 3* (InTech, 2012).
224. L. He, C. J. Evans, and A. Davies, "Optical surface characterization with the area structure function," CIRP Ann. **62**, 539–542 (2013).
225. J. C. Stover, *Optical Scattering: Measurement and Analysis*, 3rd ed. (SPIE, 2012).
226. "Standard practice for goniometric optical scatter measurements," Active standard ASTM E2387—DESIGNATION: E2387–19 (2018).
227. "Guide for angle resolved optical scatter measurements on specular or diffuse surfaces," SEMI Standard ME1392 (2015).
228. "Guide for estimating the power spectral density function and related finish parameters from surface profile data," SEMI Standard—SEMI MF1811 (2016).
229. "Test method for measuring the reflective total integrated scatter," SEMI Standard—SEMI MF1048 (2016).
230. "Optics and optical instruments—test methods for radiation scattered by optical components ICS: 31.260 Optoelectronics. Laser equipment, Technical Committee: ISO/TC 172/SC 9 Laser and electro-optical systems," ISO 13696:2002 (2002).
231. "Optics and photonics—preparation of drawings for optical elements and systems," ISO 10110.
232. P. J. Smilie and T. J. Suleski, "Variable-diameter refractive beam shaping with freeform optical surfaces," Opt. Lett. **36**, 4170–4172 (2011).
233. H. C. King, *The History of The Telescope* (1955).
234. J. P. Schaefer, "Diamond point machined snap-together optics," in *Proc. ASPE 6th Annual Meeting* (1991), pp. 70–73.
235. A. Heinrich, M. Rank, P. Maillard, A. Suckow, Y. Bauckhage, P. Rößler, J. Lang, F. Shariff, and S. Pekrul, "Additive manufacturing of optical components," Adv. Opt. Technol. **5**, 293–301 (2016).
236. B. G. Assefa, M. Pekkarinen, H. Partanen, J. Biskop, J. Turunen, and J. Saarinen, "Imaging-quality 3D-printed centimeter-scale lens," Opt. Express **27**, 12630–12637 (2019).
237. T. Gissibl, S. Thiele, A. Herkommer, and H. Giessen, "Sub-micrometre accurate free-form optics by three-dimensional printing on single-mode fibres," Nat. Commun. **7**, 11763 (2016).
238. J. Klein, M. Stern, G. Franchin, M. Kayser, C. Inamura, S. Dave, J. C. Weaver, P. Houk, P. Colombo, M. Yang, and N. Oxman, "Additive manufacturing of optically transparent glass," 3D Printing Addit. Manuf. **2**, 92–105 (2015).
239. M. Brunelle, I. Ferralli, R. Whitsitt, and K. Medicus, "Current use and potential of additive manufacturing for optical applications," Proc. SPIE **10448**, 104480P (2017).
240. A. Cannistra and T. Suleski, "Characterization of hybrid molding and lithography for SU-8 micro-optical components," J. Micro/Nanolith. MEMS MOEMS **9**, 013025 (2010).
241. A. T. Cannistra, R. A. Hudgins, and T. J. Suleski, "Fabrication and characterization of a biomimetic polarization selective lens," Opt. Lett. **37**, 1088–1090 (2012).
242. D. K. Nikolov, A. Bauer, F. Cheng, H. Kato, A. N. Vamivakas, and J. P. Rolland, "Metaform optics: bridging nanophotonics and freeform optics," Adv. Sci., submitted for publication.
243. H.-J. Mann, C. Menke, and S. Beder, "Imaging optical unit for a projection exposure apparatus," U.S. patent 9,459,539 B2 (October 4, 2016).
244. J. Lin, L. Dong, T. Fan, X. Ma, R. Chen, and Y. Wei, "Fast extreme ultraviolet lithography mask near-field calculation method based on machine learning," Appl. Opt. **59**, 2829–2838 (2020).